

StarDICE III: Characterization of the photometric instrument with a Collimated Beam Projector

Thierry Souverin¹, Jérémy Neveu^{1,2}, Marc Betoule¹, Sébastien Bongard¹, Christopher W. Stubbs³, Elana Urbach³, Sasha Brownsberger³, Pierre Éric Blanc⁴, Johann Cohen-Tanugi^{6,7}, Sylvie Dagoret-Campagne², Fabrice Feinstein⁵, Delphine Hardin¹, Claire Juramy¹, Laurent Le Guillou¹, Auguste Le Van Suu⁴, Marc Moniez², Éric Nuss^{†6}, Bertrand Plez⁶, Nicolas Regnault¹, Eduardo Sepulveda¹, Kélian Sommer⁶, and the LSST Dark Energy Science Collaboration

¹ LPNHE, CNRS/IN2P3 & Sorbonne Université, 4 place Jussieu, 75005 Paris, France

² Université Paris-Saclay, CNRS, IJCLab, 91405, Orsay, France

³ Department of Astronomy, Harvard University, 60 Garden St., Cambridge, MA 02138, USA

⁴ Université d'Aix-Marseille & CNRS, Observatoire de Haute-Provence, 04870 Saint Michel l'Observatoire, France

⁵ Aix Marseille Univ, CNRS/IN2P3, CPPM, Marseille, France

⁶ LUPM, Université Montpellier & CNRS, F-34095 Montpellier, France

⁷ LPC, Université Clermont Auvergne, CNRS, F-63000 Clermont-Ferrand, France

November 5, 2024

ABSTRACT

Context. The measurement of Type Ia supernovae magnitudes provides cosmological distances, which can be used to constrain dark energy parameters. Yet, current and upcoming large photometric surveys require a substantial improvement in the calibration precision of their photometry to reduce systematic uncertainties in cosmological constraints.

Aims. The StarDICE experiment is designed to establish accurate broadband flux references for these surveys, aiming for sub-percent precision in magnitude measurements. This requires a precise measurement of the filter bandpasses of both the StarDICE and survey instruments with sub-nanometer accuracy. To that end, we have developed the Collimated Beam Projector (CBP), an optical device capable of calibrating the throughput of an astronomical telescope and of its filters.

Methods. The CBP is built from a tunable laser source and a reversed telescope to emit a parallel monochromatic light beam that is continuously monitored in flux and wavelength. The CBP output light flux is measured using a large area photodiode, previously calibrated relative to a NIST photodiode. We then derive the StarDICE telescope throughput and filter transmissions from the CBP measurements, anchoring it to the absolute calibration provided by the NIST.

Results. After carefully analyzing the systematic uncertainties, we have achieved sub-nanometer accuracy in determining filter central wavelengths, measured each filter transmission with a precision of $\sim 0.5\%$ per 1 nm bin, and detected out-of-band leakages at the 10^{-4} relative value. Furthermore, we have synthesized the equivalent transmission for full pupil illumination from four sample positions in the StarDICE telescope mirror, with an accuracy of approximately 0.2 nm for central wavelengths and 7 mmag for broadband fluxes.

Conclusions. We have demonstrated our ability to characterize a telescope throughput down to the millimagnitude, and paved the way for future developments, such as a portable CBP version for in-situ transmission monitoring.

1. Introduction

The calibration of optical wide-field surveys needs to reach new levels of precision to meet the requirements of type Ia supernovae (SNe Ia) cosmology. SNe Ia are standard candles, a class of objects with predictable luminosity used as probes to characterize dark energy in the late Universe. We can infer dark energy properties by measuring the luminosity distance of SNe Ia at different redshifts. This luminosity distance is obtained by measuring the maximum amplitude of the SN Ia light curve, which is observed within different optical bands depending on its redshift. Errors in the relative flux calibration between the different bands have a knock-on effect on systematic errors in the Hubble diagram, which are then propagated to dark energy parameters constraints.

Current photometric surveys like the Dark Energy Survey (DES) (Brout et al. 2019) or Subaru Hyper Suprime-Cam (HSC) (Yasuda et al. 2019) observed hundreds of SNe Ia. The Zwicky Transient Facility (ZTF) (Dhawan et al. 2022) should total up to about 10 000 spectroscopically confirmed SNe Ia, a consequent increase compared to previous surveys. Joint analysis has been

performed to benefit from the different existing surveys, reducing the statistical uncertainty on the measurement of cosmological parameters (Betoule et al. 2014; Scolnic et al. 2018; Brout et al. 2022; Rubin et al. 2023). Additionally, we expect the SNe Ia catalog to reach a new order of magnitude within the next decade thanks to the Legacy Survey of Space and Time (LSST) undertaken by the Vera Rubin Observatory (LSST Science Collaboration et al. 2009), which is expected to observe between 120,000 and 170,000 SNe Ia up to redshifts $z \sim 0.3$ (Lochner et al. 2022). With this tremendous increase, the statistical uncertainty on cosmological parameters will consequently diminish, leaving the photometric calibration as one primary source of systematic uncertainty. Therefore, the photometric calibration needs to reach sub-percent precision to benefit from the incoming statistics of the present and future surveys.

SNe Ia survey bandpasses are calibrated relatively to the CALSPEC catalog of spectrophotometric standard stars (Bohlin et al. 2020), which relies on the radiative transmission model of white dwarf atmospheres (Narayan et al. 2019). To transfer this calibration to the photometric survey, it is necessary to consider two additional components: (i) the terrestrial atmospheric

transmission and (ii) the survey filter transmissions as a function of wavelength, with particular attention given to the bandpasses edges wavelength position. The former can be inferred by airmass regression with observations of CALSPEC reference stars or by slitless spectrophotometric analysis with a dedicated telescope such as the Rubin Observatory’s auxiliary telescope (AuxTel), as detailed in [Neveu et al. \(2024\)](#). The latter needs beforehand precise measurements of the bandpasses throughput. Multiple strategies have been developed to provide this measurement on different surveys. The most common approach consists of using calibrated sensors such as the ones supplied by the National Institute of Standards and Technologies (NIST) ([Houston 2008](#)) to monitor a light source used to illuminate a telescope to measure its throughput and filter transmissions. Several approaches involve diffusion on a flat-field screen toward the instrument ([Stubbs & Tonry 2006](#); [Marshall et al. 2013](#)). Other designs have been developed, like [Lombardo et al. \(2017\)](#), which involves integrating spheres and parabolic mirrors to redirect the light in a parallel beam.

The StarDICE experiment ([Betoule et al. 2023](#)) proposes a metrology chain from laboratory flux references toward the measurement of standard star spectra. Several steps are needed to calibrate increasingly sensitive detectors and finally transfer this calibration to on-sky sources. The StarDICE 40 cm diameter telescope is calibrated with a stable light source positioned far enough (~ 100 m) to appear as a pointlike source and provides in-situ calibration of the instrument. Composed of LEDs, the calibrated light will emit broadband flux, which will be used to monitor the *ugrizy* filters of the StarDICE telescope at the millimagnitude level. Beforehand, it is necessary to have a laboratory measurement of the filter transmission at high wavelength resolution to interpret the broadband LED and star measurements. In this context, a Collimated Beam Projector (hereafter CBP) has been developed to accurately measure the StarDICE telescope response $R_{\text{tel}}(\lambda)$, including the optics, the CCD camera quantum efficiency, and the filter transmission.

The CBP was initially designed for the LSST telescope ([Ingraham et al. 2016](#)), and prototypes have been used to measure the throughput of the CTIO 0.9 m telescope and the DECam wide field imager, respectively, in [Coughlin et al. \(2018\)](#) and [Coughlin et al. \(2016\)](#). Compared to flat-field illumination devices, the CBP can project monochromatic light in a collimated beam, which provides parallel monochromatic illumination over a portion of the primary mirror. A first prototype of the CBP for StarDICE has been developed in [Mondrik et al. \(2023\)](#) as a proof-of-concept and measured the instrument throughput with a precision of $\sim 3\%$ for wavelengths between 400 nm and 800 nm, and a wavelength calibration estimated at ~ 0.2 nm.

This paper details the enhanced version of the StarDICE CBP, now equipped with a tunable laser as a monochromatic source that injects light at the focal point of a Ritchey-Chrétien telescope mounted backward. The output light of the CBP is collimated and illuminates the StarDICE telescope pupil to measure its throughput. Combining the calibration effort provided by [Houston \(2008\)](#) and [Brownsberger et al. \(2022\)](#) for the detectors and all the lessons learned from previous prototypes, we aim at measuring the StarDICE telescope throughput and *ugrizy* filter transmissions at the sub-percent level. The other goal is to confirm the wavelength calibration accuracy of 0.2 nm. This study has two major intents: (i) to provide a first measurement of the StarDICE filter transmission to contribute to the metrology chain of the experiment, and (ii) to serve as a pathfinder for the future measurement of the LSST telescope with its dedicated version of the CBP.

The following sections of the paper are structured as follows: Section 2 presents the laboratory setup of the experiment and gives an overview of the campaign of measurements. Section 3 details the measurements of the CBP optics response. Section 4 presents the obtained measurements of StarDICE telescope throughput and filter transmissions. The StarDICE full-pupil synthesizing methodology and main results are presented in Section 5 and discussed in Section 6.

2. Laboratory setup

Our setup consists of three primary components: the StarDICE telescope, a large area photodiode employed as a calibration reference, and the CBP that illuminates one or the other. The following section will describe each component and detail its operations.

Compared to the original CBP design outlined in [Mondrik et al. \(2023\)](#), a significant enhancement is using a solar cell to calibrate and monitor the CBP optical transmission between the optical sphere and the telescope output. Other noteworthy improvements include (1) replacing the laser light source from NIST with an EKSPLA NT 252, which offers a slightly more favorable wavelength power cutoff, (2) implementing a filtering system to prevent laser harmonics from being injected into the light beam and (3) synchronizing the photocurrent readings with laser light emission, facilitating the extraction of the signal, (4) replacing the Hasselblad camera by a Ritchey-Chrétien telescope as collimating optics to remove all chromatic effects and enlarge the illumination region.

2.1. StarDICE

The StarDICE photometric instrument consists of a Newton telescope with a primary mirror of 40 cm diameter (16”) and 1.6 m focal length ($f/D = 4$). The focal plane hosts an Andor Ikon-M DU934P-BEX2-DD camera equipped with a deep depleted, back-illuminated CCD sensor (E2V DU934P). The active area of the sensors is 13.3 mm \times 13.3 mm divided in 1024 \times 1024 square pixel of 13 μ m side. In this baseline setup, the pixel resolution is 1.68” and the field of view 28.6’ \times 28.6’. “ugrizy” A 9-slots 28.5 mm filter wheel positioned in front of the camera features 6 interference filters in the *ugrizy* photometric system, a Star Analyser 200 diffraction grating, and a 0.2 mm pinhole. The remaining slot is left empty. Aside from the optional filters, the only other glass part in the light path is the non-coated fused-silica window of the CCD cell¹. A 0.5° wedge affects the window’s two sides.

The z-position of the camera-filter wheel assembly is adjustable over 9 cm, allowing to focus from distances as close as 35 m up to infinity. The secondary mirror, with a diameter of 11 cm, is oversized to ensure the fully-illuminated plane extends over the sensor with a comfortable margin in all optical configurations.

In operation, the camera sensor is thermoelectrically cooled down to a temperature of -70 °C, delivering a median dark current of 0.15 e⁻/s, neglected for the ~ 1 s exposures considered in this study. When operated in the lab, the telescope was mounted on a custom altazimuth mount to enable easy alignment with the CBP.

¹ The manufacturer code for this window is WN35FS(BB-VV-NR)W

2.2. Collimated Beam Projector

The Collimated Beam Projector (CBP) general setup requires the following components: a tunable monochromatic light source and an optic device able to recreate a parallel beam from a point source. In our case, the light source is an Ekspla NT252 tunable laser, using a Q-switched pump laser at 1064 nm and non-linear crystals to produce powerful monochromatic pulses from 335 to 2600 nm. The pulse duration is fixed and lies between 1 and 4 ns with an energy of 1.1 mJ in the near-infrared. The energy can be decreased at will by a factor of 2 using the tuning of the Q-switch (namely QSW in the following), degrading the resonant cavity's quality factor. Pulses are shot with a fixed frequency of 1 kHz and can be shot in two modes. The first one is called the "continuous mode", since it shoots pulses continuously with a 1 kHz frequency, while the second one is called "burst mode", sending packets of pulses by bursts. Each burst is composed of 1 to 1000 pulses, meaning the duration of a burst is restrained between 1 ms and 1 s. The pulses have a maximum linewidth below 10 cm^{-1} , which can be converted into a maximum spectroscopic width below 0.4 nm around 600 nm. This is an upper limit quoted by the manufacturer, but measurements taken using a similar laser show bandwidths going from 0.08 nm to 0.48 nm in the 350 to 1100 nm range (Woodward et al. 2018). The standard deviation of pulse energy is around 2.5%. This laser is composed of three different operational configurations, from 335 to 669 nm, from 670 to 1064 nm and above 1064 nm, which results in three different regimes of power and light contamination in the CBP. This laser was chosen for its wide wavelength range and the high pulse energy, as the source power is a crucial criterion for CBP calibration with the solar cell, our reference calibration photodiode (see Section 2.3).

The laser output is polluted by light from the pump laser of other resonances in the system, both spatially and chromatically. The spatial pollution is stopped with a diaphragm. On the other hand, a filter wheel that contains three different broad bandpass filters purifies the laser light from pump photons or another parasite signal. In particular, we use a red-pass filter RazorEdge LP03-532RU-25 to filter out the 532 nm pump photons in the regime 645 to 1074 nm, and a infrared-pass filter RazorEdge LP02-1064RU-25 above 1074 nm to filter $< 1064 \text{ nm}$ photons appearing in this regime. We also use a blue-pass filter Bright-Line Multiphoton FF01-680/SP-25 in the regime 530 to 645 nm to remove contamination not detected in the spectrograph and which we were not able to identify. A black metallic box encloses the entire optical stage to minimize light scattering in the room.

Being filtered, the light is focused and injected into an optical fiber Thorlabs MHP910L02 with a wide core diameter of $910 \mu\text{m}$, which is plugged into an IS200-4 $\Phi 2''$ integrating sphere from Thorlabs, which has an internal 50 mm diameter and is composed of 1 input and 4 output ports. The integrating sphere dilutes the flux, breaks the laser light coherence, and eliminates any spatial dependence to achieve a uniform surface brightness. Two monitoring instruments are plugged into the sphere. First, a silicon photodiode Thorlabs SM05PD3A with high efficiency in the UV is mounted on an output port orthogonal to the laser input port to control the laser power stability. It is mounted behind a pinhole to reduce the photon flux and ensure it works in its linear regime. It is read by a Keithley 6514 electrometer at a rate of 50 Hz. Additionally, an OceanOptics QE65000 fiber spectrograph is plugged into another output to monitor the true laser wavelength and spectral purity. One port is left free to plug a calibration lamp to calibrate the spectrograph when needed. Fi-

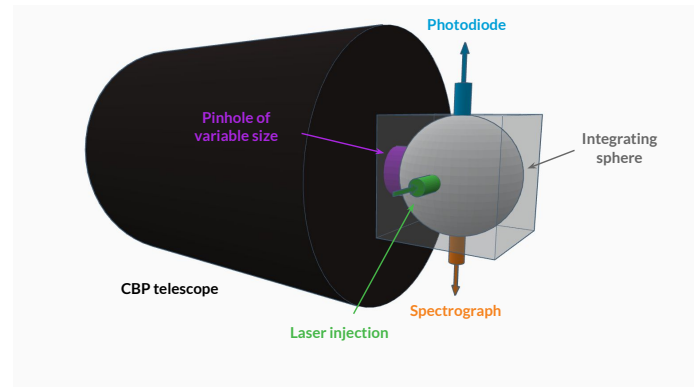


Fig. 1: Schematic of the integrating sphere

nally, a slider with pinholes of different diameters is mounted on the output port connected to the CBP optics. Figure 1 shows a schematic of the integrating sphere and the instruments plugged into it.

We used three different pinholes, of diameter $75 \mu\text{m}$, 2 mm (respectively P75HK and P2000HK from Thorlabs) and 5 mm (homemade). The 5 mm pinhole is the largest possible given the StarDICE field of view and gives the maximum flux. The other pinholes are used for systematic checks and filter edge analysis. The pinhole slider is attached to the ocular of a 154/1370 Ritchey-Chrétien Omegon telescope to position the pinhole at the focal point of the optics. The light injected in the telescope mounted backward will project a parallel and collimated beam. An iris diaphragm is positioned 16 mm after the pinhole and adjusted to cut light that would otherwise miss the telescope's secondary mirror. A small amount of light scatters on the iris blades, best observed in telescope images of the CBP taken with the 2 mm pinhole configuration. In these images, it forms a faint ring with a radius of approximately 340 pixels, distinct from the main spot. When comparing the annular photometry of the ring to that of the main spot, the fraction of scattered light is usually smaller than 6×10^{-4} between 400 and 900 nm.

The assembly is mounted on a robotic Celestron NexStar Evolution 6 altazimuth mount. As a last step, we cropped the output of the Ritchey-Chrétien Omegon with a mask shaped as a quarter of a disk corresponding to one quadrant of its secondary mirror spider so that the actual beam shape is only a fourth of the complete aperture. This ensures that the entire beam can fit inside the reference solar cell footprint.

2.3. Solar cell description

We use a C60 solar cell of 3rd generation from Sunpower as our calibration reference. Its sensitive area forms a square with 12.5 cm side, setting the maximum size of the CBP beam, which can be accurately calibrated. This solar cell is set on a two-axis mount, one that allows a movement in the direction of the optical axis of the CBP telescope and another vertical axis, which allows the adjustment of the height of the solar cell. It is placed at 16 cm approximately from the telescope aperture. This solar cell is connected via a coaxial cable to a Keysight B2987A electrometer, the same that was used for its calibration. The charges are measured at a rate of 500 Hz. In Figure 2 right, we show a picture of the setup when the CBP is aiming at the StarDICE telescope described in section 2.1.

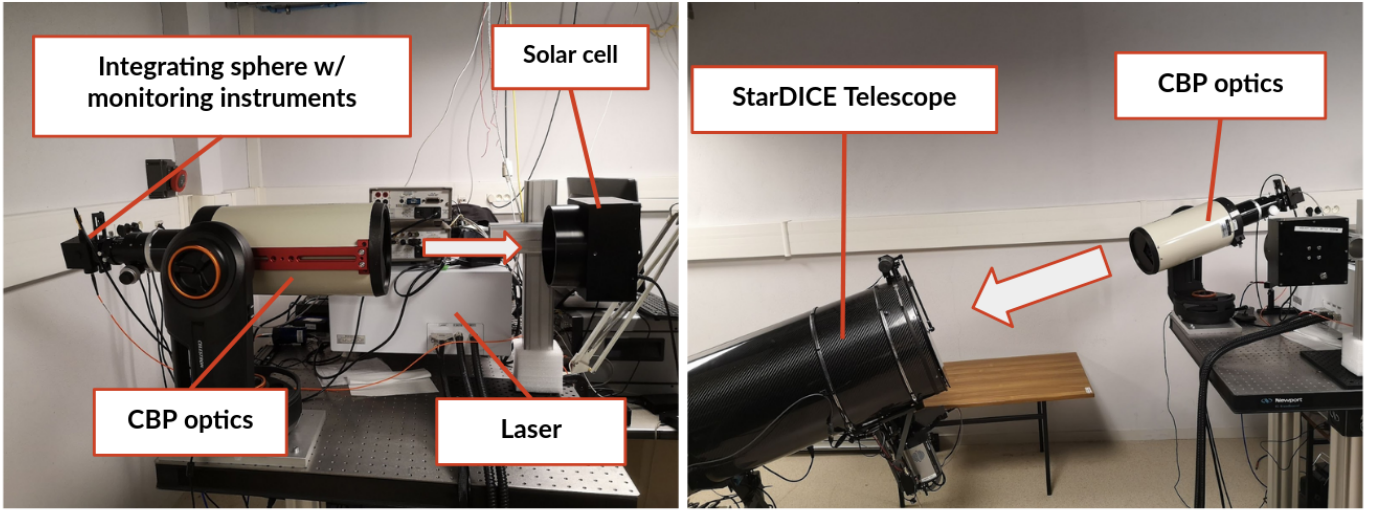


Fig. 2: Pictures of the different CBP setups. Left: CBP setup when shooting in the solar cell. Right: CBP setup when shooting in the StarDICE telescope.

2.3.1. Quantum efficiency measurement

The quantum efficiency (QE) as a function of wavelength for the solar cell was measured relative to a NIST-calibrated photodiode by using a monochromator as a light source and using an electrometer to measure the current of the solar cell and of the photodiode at each wavelength. The monochromator wavelength was calibrated with a spectrograph relative to a mercury calibration source. Details of the setup are discussed in Brownsberger et al. (2022). The quantum efficiency of the solar cell used for these measurements is shown in Fig. 3. Five measurements were taken per source wavelength with a 1 nm step. The smoothed average per wavelength is reported in Fig. 3. The cited uncertainty arises from the RMS of the current measurements. The glitch at ~ 550 nm caused by inserting a 550 nm long pass filter to cut off second-order light contamination is masked by a linear interpolation.

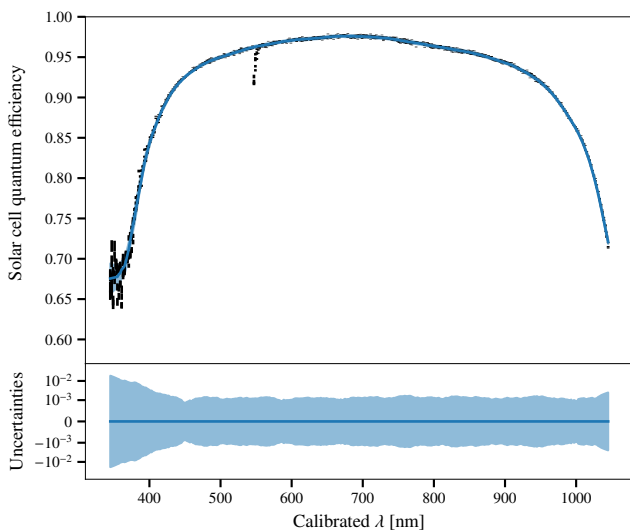


Fig. 3: Solar cell quantum efficiency with respect to wavelength (top) and error bar sizes (bottom).

The QE of the solar cell was measured within a temperature range from 32°C to 39°C . The QE increased slightly at longer wavelengths as the temperature increased (see Fig. 4). This trend is consistent with the temperature dependence of silicon's QE (Green 2008). At 1050 nm, the QE changes by more than 0.1 percent per degree.

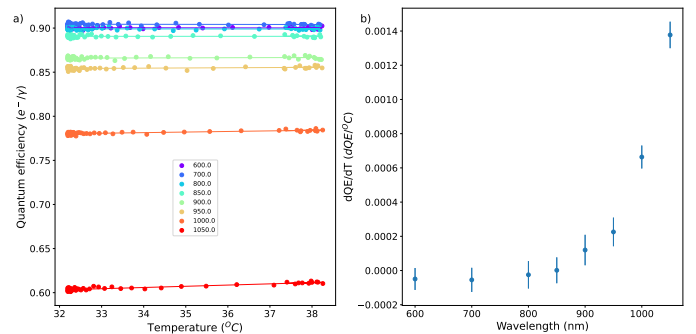


Fig. 4: (a) Solar cell quantum efficiency vs temperature for wavelengths ranging from 600 to 1050 nm. (b) Fitted change in quantum efficiency per degree Celsius for wavelengths ranging from 600 to 1050 nm.

The effect of the angle of incidence on the solar cell QE was also measured. The solar cell was rotated up to 35 degrees off-axis. The results are shown in Fig. 5. There is a stronger dependence on the incidence angle at wavelengths less than 600 nm, but the change in QE for wavelengths greater than 400 nm is less than 5×10^{-4} per degree.

The solar cell was aligned perpendicularly to the CBP output beam with a precision better than 1° and has not been moved throughout the entire measurement campaign. Meanwhile, room temperature was monitored and has not varied more than 2°C .

2.3.2. Dark current characterization

Due to the low resistance of the solar cell, we observed a relatively high current of approximately 20 nA even in dark conditions. Therefore, we built a device that uses a precision voltage

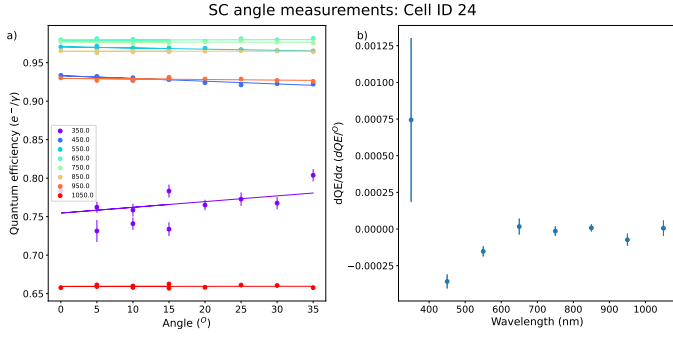


Fig. 5: (a) Solar cell quantum efficiency vs solar cell tilt relative to normal incidence for different wavelengths. (b) Fitted change in quantum efficiency per degree of solar cell tilt relative to normal incidence vs wavelength.

source with a tunable voltage divider to inject a counter-current that cancels this contribution. The current value was tuned to observe approximately no drift when using the Keysight in charge mode inside the usual acquisition time window (< 1 min). In doing so, we avoided saturating the electrometer when using the solar cell in dark and laser-on conditions.

After canceling the dark current drift, the power spectrum of the solar cell dark current revealed a $1/f$ noise, with power line harmonics contributions at 50 Hz, 100 Hz, and 150 Hz (see Figure 6). To investigate the source of the $1/f$ component in the power spectrum, we compared the output of the Keysight when connected to a resistor with the same value as the shunt resistance of the solar cell. We found that the two power spectra were identical, leading us to conclude that the fluctuations in the trans-impedance amplifier bias voltage are the source of this $1/f$ noise. These fluctuations cause parasitic currents to flow through the load resistance. By increasing the load resistance, we can decrease the amplitude of the resulting noise. Among a set of calibrated solar cells, we therefore chose the one with the highest shunt resistance at our disposal ($R_{\text{shunt}} = 1.8 \text{ k}\Omega$) and limited the burst durations to at most 200 pulses (200 ms). In doing so, in the burst time window, the Keysight noise is dominated by the power line harmonics, whereas the random $1/f$ noise remains subdominant.

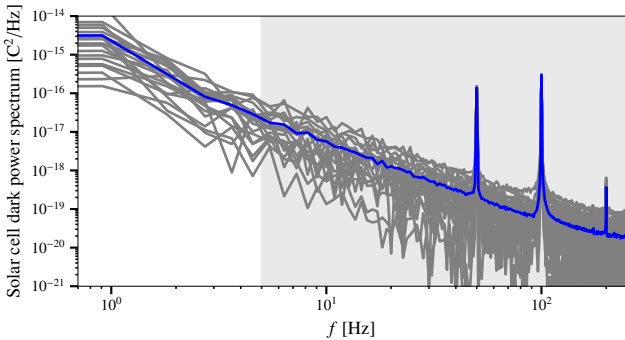


Fig. 6: Solar cell dark current power spectrum for 20 runs without light in the solar cell (gray curves) and their averages (blue). The light gray region encompasses the expected noise spectrum contribution for 200 ms laser bursts.

Table 1: Definition of measured quantities in our StarDICE +CBP setup.

Name	Description
$Q_{\text{phot}}(\lambda)$ [C]	The charge per burst collected by the integrating sphere monitoring photodiode, measured by the Keithley 6514.
$Q_{\text{solar}}(\lambda)$ [C]	The charge per burst collected by the solar cell, measured by the Keysight 2987A.
$Q_{\text{ccd}}(\lambda)$ [ADU]	The charge collected by the Andor CCD camera of the StarDICE telescope.

2.4. Time synchronisation

The precision of the analysis is significantly improved if the laser pulses can be accurately identified within the photocurrent time series. This is particularly crucial for solar cell measurements, where signal-to-noise ratios are typically lower.

To accomplish such synchronization, we recorded the timing of all three trigger lines of the laser and both electrometers on a single microcontroller. Upon detecting a TTL pulse on any of these lines, the microcontroller registers a 32-bit timestamp using its internal clock counter, enabling synchronization with a resolution of 500 nanoseconds over extended durations (up to 2100 seconds). This custom synchronization device, Arduino-based, whose code is openly accessible [Betoule \(2022\)](#), is referred to as the digital analyzer throughout the remainder of this text.

2.5. Measurement principle

Table 1 summarizes the three quantities measured with the two setups in Figure 2.

First, we need to measure the response of the CBP optics $R_{\text{CBP}}(\lambda)$ by shooting into the calibrated solar cell as shown in Figure 2 left. It is computed with the Equation 1. In this equation, we know the quantum efficiency of the solar cell ϵ_{SC} from Figure 3, and e is the elemental charge of the electron.

$$R_{\text{CBP}}(\lambda) = \frac{Q_{\text{solar}}(\lambda)}{Q_{\text{phot}}(\lambda) \times \epsilon_{\text{SC}} \times e}. \quad (1)$$

Once we have this response, we can shoot inside the StarDICE telescope as shown in Figure 2 right, and obtain $R_{\text{tel}}(\lambda)$ with the Equation 2.

$$R_{\text{tel}}(\lambda) = \frac{Q_{\text{ccd}}(\lambda)}{Q_{\text{phot}}(\lambda) \times R_{\text{CBP}}(\lambda)}. \quad (2)$$

We will focus on $R_{\text{CBP}}(\lambda)$ and $R_{\text{tel}}(\lambda)$ respectively in sections 3 and 4.

2.6. Measurement overview

The schedule for all measurements conducted to determine $R_{\text{tel}}(\lambda)$ and estimate associated systematic uncertainties is outlined in Table 2. Each row in the table corresponds to a specific hardware configuration and measurement run. We have assigned labels to each run and specified the following details: (1) the target of the CBP, (2) the pinhole used in the CBP slide, (3) the QSW setting for the laser, (4) the filters used in the StarDICE camera filter wheel (when applicable), (5) any specificity of the measurement, and (6) the number of runs.

The measurement campaign has started and ended with a calibration of the spectrograph. A calibration Hg-Ar lamp was plugged into the integrating sphere, and its light was measured using a spectrograph. This corresponds to lines No. 1 and No. 13 of the Table 2.

Two different pinholes in the CBP slides were used for these measurements. When shooting into the StarDICE telescope, the 75 μm pinhole forms a point-like image of about 10 pixels in diameter well suited for photometry while avoiding issues related to ghosting. When shooting into the solar cell, the 5 mm pinhole is necessary to achieve a good signal-to-noise ratio. Since $R_{\text{CBP}}(\lambda)$ depends slightly on the pinhole diameter, we also need to intercalibrate the two responses $R_{\text{CBP}}^{5\text{mm}}(\lambda)$ and $R_{\text{CBP}}^{75\mu\text{m}}(\lambda)$. This inter-calibration can be performed thanks to the measurements in line No. 8 of Table 2.

A significant issue with the CBP is that its output light does not illuminate the entirety of the StarDICE primary mirror as an astrophysical source would do, but only a portion of it. It is necessary to perform a *pupil stitching* to reconstruct the transmission of the mirror by combining the measurement of $R_{\text{tel}}(\lambda)$ when shooting at different positions on the mirror. Only the point of impact on the mirror is modified when doing so, but the point of incidence on the focal plane is the same. The different positions are shown in Figure 7. The pupil stitching corresponds to lines No. 2 and No. 3 of Table 2. The method used to perform the pupil stitching is detailed in Section 5.

To check the uniformity of the StarDICE focal plane, a measurement of $R_{\text{tel}}(\lambda)$ at 16 different positions on the focal plane has been performed. Only the position on the focal plane is modified, while the point of impact on the mirror stays the same. This dataset corresponds to the line No. 12 of Table 2.

Finally, some systematic measurements have been carried out. A cap has been placed on the CBP output to measure the room's background for both setup configurations, corresponding to lines No. 9 and No. 10 of Table 2. A measurement of the scattered light is possible with dataset No. 11 by shifting the position of the solar cell from the CBP output of approximately 16 cm.

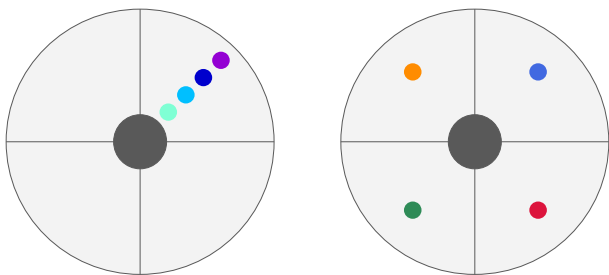


Fig. 7: Left: Schematic of the 4 different radial relative positions on the primary mirror of the StarDICE telescope. Right: Schematic of the 4 different quadrant relative positions on the primary mirror of the StarDICE telescope.

3. CBP response calibration with a solar cell

3.1. Optics setup

The CBP optics have two degrees of freedom that must be adjusted before determining its transmission: (1) the focuser dis-

tance, which needs to be tuned so that the pinhole is at the focal plane of the telescope and produces a collimated beam; and (2) the size of the iris diaphragm, which needs to be adjusted so that no light misses the CBP secondary mirror.

To adjust the focuser distance, we re-imaged the CBP pinhole in the StarDICE camera using the StarDICE telescope set up for infinity focus. We then adjusted the CBP focus to minimize the size of the image in the camera and tightened the locking screws. We checked that the focus was reasonably stable regarding manual changes of the pinhole slots.²

To adjust the size of the iris diaphragm, we incrementally closed it while monitoring the flux output of the CBP. A decrease in flux signaled that the diaphragm was beginning to block collimated light. Continuing to close the diaphragm would only reduce the transmission of the CBP without additional advantages in minimizing scattered light. Therefore, we set the diaphragm at this optimal point and secured it to maintain stable CBP transmission.

3.1.1. Alignment of the CBP

To measure the CBP response, we must ensure that we aim toward the solar cell. For that, we studied the signal collected in the solar cell $Q_{\text{solar}}^{\text{mes}}$ with respect to the CBP mount coordinates in azimuth and altitude. When no measurements are taken, the parking coordinates of the CBP are set as (alt = 0°, az = 0°), and the coordinates in the Figure 8 are relative to this origin. With this figure, we can estimate the coordinates at which $Q_{\text{solar}}^{\text{mes}}$ is maximum, corresponding to the solar cell coordinates in the CBP mount frame of reference. Thus we set the solar cell coordinates at (alt = 6°, az = 10°), corresponding to the point aimed by the CBP optics for any further solar cell analysis in this paper.

3.2. Description of the CBP data set

A typical dataset to measure the CBP response is the emission of laser bursts in the solar cell at a given wavelength. Charges in the photodiode and solar cell are recorded jointly, along with the flux in the spectrograph and the time stamps in the digital analyzer (see examples in Figure 9).

The laser emits pulses at a fixed rate of 1 kHz, with a power that highly depends on the wavelength. To ensure that all instruments work in their linear regime without saturation and to limit the impact of dark current fluctuations, we decided to shoot light in the solar cell in bursts of pulses separated by dark times at least as long as the burst length. The photodiode being the instrument in common for all our measurements, the number of pulses per burst at each wavelength was adjusted to minimize the change in total flux per burst collected in the photodiode over the entire wavelength range (Figure 10). With the 5 mm pinhole and the largest laser power mode, the solar cell accumulates around 4 nC in a burst. To keep the $1/f$ noise of the solar cell instrumental chain under reasonable bounds, we limited

² While this procedure ensures that the two instruments are perfectly conjugated, an error in the focus of one is compensated by an error in the focus of the other. As this procedure was conducted before the first stellar light of the StarDICE telescope, we had to use a theoretical value for its focal plane position, which proved to be about 2 mm behind its actual focal point. As a result, we estimate that the collimated beam was diverging by about 2 mrad. While inconsequential on the transmission measurement itself, the uncertainty on the exact optical arrangement has a practical side effect on the data taking because it affects the ghosting pattern which we intended to use to determine the CBP spot position on the StarDICE mirror see the discussion in Sect. 5.1

Table 2: Detailed schedule of the measurements.

N°	Label	Target	Pinhole	QSW	StarDICE bands	Specificity	Number of runs
1	Wavelength calibration	Spectrograph	-	-	-	Hg-Ar lamp light source	1
2	Radial pupil stitching	StarDICE	75 μ m	MAX	u, g, r, i, z, y, EMPTY, GRATING	4 mirror radial positions	1 per position
3	Quadrant pupil stitching	StarDICE	75 μ m	MAX	EMPTY	4 mirror quadrant positions	1 per position
4	Repeatability measurement	StarDICE	75 μ m	MAX	u, g, r, i, z, y, EMPTY, GRATING	Fixed mirror and focal plane position	3
5	CBP response calibration before	Solar cell	5 mm	298, MAX	-	CBP monitoring before StarDICE measurements	5
6	StarDICE main calibration	StarDICE	5 mm	MAX	u, g, r, i, z, y, EMPTY, GRATING	Fixed mirror and focal plane position	5
7	CBP response calibration after	Solar cell	5 mm	298, MAX	-	CBP monitoring after StarDICE measurements	5
8	Pinholes inter-calibration	StarDICE	75 μ m, 2 mm, 5 mm	MAX	EMPTY	3 different pinhole sizes	1 per pinhole
9	StarDICE background measurements	StarDICE	5 mm	MAX	EMPTY	Cap on CBP output	1
10	Solar cell background measurements	Solar cell	5 mm	MAX	-	Cap on CBP output	2
11	Solar cell distance calibration	Solar cell	5 mm	298, MAX	-	2 solar cell positions at 16 cm relative distance	1 per position
12	Focal plane measurement	StarDICE	75 μ m	MAX	EMPTY	4x4 grid positions on the StarDICE focal plane	1 per position
13	Wavelength calibration	Spectrograph	-	-	-	Hg-Ar lamp light source	1

the maximum length of a burst to 200 ms. The CBP system's linearity is checked by varying the laser power as discussed in Section 3.6.5. The required total flux in the photodiode was then adjusted by accumulating several bursts measured independently by the solar cell.

During a solar cell measurement run, the laser wavelengths range between 350 nm and 1100 nm included with steps of 1 nm, but are randomly chosen to avoid that long-range $1/f$ mode in the solar cell dark current correlates neighbored data points of the CBP response. Several runs were accumulated to enhance the signal-to-noise ratio. In particular, five runs (dataset No. 4 from Table 2) were recorded just before the StarDICE telescope measurement (dataset No. 5), and five new runs (dataset No. 6) were launched just after.

Runs with different settings have been conducted to estimate systematic uncertainties. We varied the laser global power (QSW) to assess the linearity of the instrumental light (dataset No. 4 and 6). Additionally, we checked the ambient light additive contamination (dataset No. 10) and varied the solar cell distance to estimate the output CBP scattered light (dataset No. 11).

3.3. Spectrograph data analysis

In our analysis, the spectrograph is used to monitor the laser wavelength and the contamination of extra emission lines in addition to the main laser line. The main components of the contamination are a 532 nm half harmonic and a 1064 nm line from the Yagg laser pump. In the following subsection, we detail the wavelength and flux calibration procedures for this instrument

and leave the discussion of the light contamination to section 3.3.4

3.3.1. Spectrograph data reduction

The spectrograph was characterized by taking a series of dark exposures with four different exposure times (the same used in the CBP response measurement) to evaluate its gain and readout noise. The goal is to build an error model for the spectrograph.

For each exposure time, a master dark is constructed, averaging all the spectra. Then, for each spectrograph pixel, we fitted a line through the master dark values as a function of the exposure times. The intercept gave the sensor bias value for each pixel, and a master bias $B(\lambda_p)$ is assembled from the intercept values (corresponding to null exposure time), with λ_p the raw spectrograph wavelength value before any calibration associated with each sensor pixel p .

The spectrograph could not be synchronized with the laser bursts. Therefore, for a given laser burst, we get spectra with different amplitudes depending on the number of pulses read by the spectrograph (see bottom row Figure 9. All spectra are stacked into a curve $S(\lambda_p)$ to get the maximum signal to noise.

We locally fit Gaussian profiles on top of a linear background to detect emission lines in $S(\lambda_p)$. Let's call λ_g the line centroid fitted by this Gaussian profile. The fit is unweighted to avoid any dependence of λ_g with the line flux, and we verified it was the case.

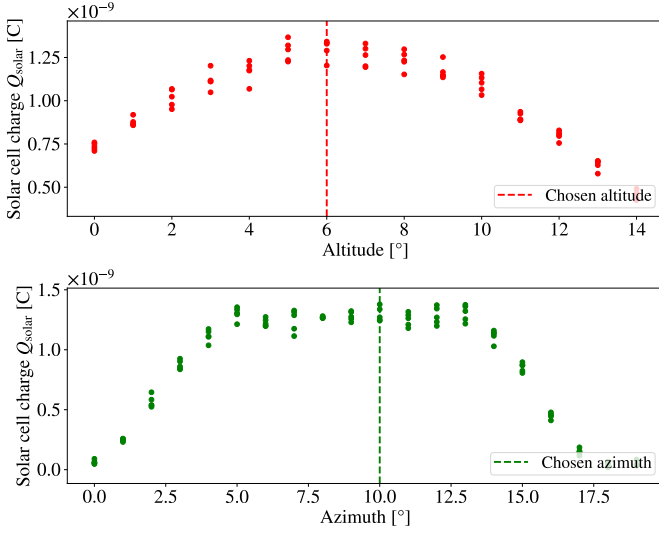


Fig. 8: Alignment scan showing the evolution of the beam intensity in the solar cell ($Q_{\text{solar}}^{\text{mes}}$) as a function of the two coordinates of the CBP mount: altitude (top panel) and azimuth (bottom panel). A flux plateau indicates the region where the entire beam is contained within the cell footprint. The wider plateau in azimuth is due to the smaller extent of the beam in the horizontal direction due to the shape and orientation of the masked output pupil.

The Gaussian profile fit is unweighted, but a statistical uncertainty $\sigma_{\lambda}^{\text{noise}}$ is still estimated for λ_g as

$$\sigma_{\lambda}^{\text{noise}} = \frac{1}{\sum_p F_p} \sqrt{\sum_p (\lambda_p - \lambda_g)^2 F_p} \quad (3)$$

with F_p the flux in pixel p after master bias subtraction. The sums are performed over a window of size $\pm 3\sigma_g$ around λ_g where σ_g is the fitted line Gaussian profile RMS. Equation 3 corresponds to the propagation uncertainty formula for the average wavelength weighted by flux F_p in a $\pm 3\sigma_g$ window around λ_g . This allows us to consider the shot noise without biasing the λ_g fit.

An example of a stacked spectrum with the detection of the laser line at 643 nm and the pump line at 532 nm is shown in Figure 11, before spectrograph wavelength calibration.

3.3.2. Spectrograph wavelength calibration

We calibrated the spectrograph according to the manufacturer's specifications before and after the main data acquisition run to measure the CBP and StarDICE responses. Light from a Hg-Ar lamp was injected into the integrating sphere to illuminate the spectrograph sensor. The spectral lamp data were reduced as described in Section 3.3.1.

To transform raw sensor wavelengths λ_p into calibrated wavelengths λ_c , we fitted a third-order polynomial function as suggested by the manufacturer to minimize the distance to Hg-Ar tabulated values λ_r . This was done by minimizing the following function:

$$\chi_{\lambda}^2(a_3, a_2, a_1, a_0) = \sum_{\text{lines}} \frac{(\lambda_r - a_3\lambda_p^3 - a_2\lambda_p^2 - a_1\lambda_p - a_0)^2}{(\sigma_{\lambda}^{\text{noise}})^2} \quad (4)$$

over the four polynomial coefficients a_3, a_2, a_1 and a_0 . The sum is performed over lines with high significance (signal-to-noise ratio above 20), and known doublet lines were excluded. Lines are weighted according to their signal to noise. The minimization yields the four best-fit parameters \hat{a}_i associated with their covariance matrix \mathbf{C}_a . As the initial Gaussian fit was unweighted, the covariance matrix \mathbf{C}_a is then re-scaled with a global factor r such as we get a final reduced χ_{λ}^2 of one. Finally, detected line centroids λ_g are transformed into calibrated wavelengths λ_c using the third order polynomial function $c(\lambda_g)$ with the four best fit parameters:

$$\lambda_c \equiv c(\lambda_g) \equiv \hat{a}_3\lambda_g^3 + \hat{a}_2\lambda_g^2 + \hat{a}_1\lambda_g + \hat{a}_0 \quad (5)$$

and the $\sigma_{\lambda}^{\text{cal}}$ calibration uncertainties are

$$\sigma_{\lambda}^{\text{cal}} = (r\mathbf{J}_a^T \mathbf{C}_a \mathbf{J}_a)^{1/2}, \quad \mathbf{J}_a = (\lambda_g^3, \lambda_g^2, \lambda_g, 1). \quad (6)$$

In Figure 12, we plot the residuals of the fit $c(\lambda_g) - \lambda_t$ in the upper panel, showing the agreement between the re-scaled data uncertainties and the uncertainties propagated to the third order polynomial function $c(\lambda_g)$ using \mathbf{C}_a . In the lower panel, the spectrograph calibration systematic uncertainties $\sigma_{\lambda}^{\text{cal}}$ are emphasized: they are lower than 0.1 nm in the entire wavelength range, even lower than 0.025 nm in the visible spectrum.

3.3.3. Laser wavelength calibration

We reduce all spectrograph data sets to calibrate laser wavelengths following the recipe in Section 3.3.1.

We applied the third-order polynomial $c(\lambda_g)$ to transform λ_g sensor wavelengths into calibrated wavelengths λ_c . We used the 532 nm line to check the quoted statistical errors $\sigma_{\lambda}^{\text{noise}}$ on wavelength. We plotted the fitted 532 nm line position versus time for all data sets. The RMS is compatible with the quoted error bars on wavelength for lower signal-to-noise ratio data sets. However, for the high signal-to-noise ratio data sets, some dispersion was unaccounted for, which is explained by the fact that the Gaussian profile is an incomplete model for high signal-to-noise lines. Therefore, we added a $\sigma_{\lambda}^{\text{PSF}} = 0.012$ nm statistical uncertainty attributed to PSF modeling on wavelength uncertainty $\sigma_{\lambda}^{\text{noise}}$ to get a normal distribution for the residuals normalized by the full statistical uncertainties (see Figure 13), the latter being

$$(\sigma_{\lambda}^{\text{stat}})^2 = (\sigma_{\lambda}^{\text{noise}})^2 + (\sigma_{\lambda}^{\text{PSF}})^2. \quad (7)$$

Finally, the wavelength uncertainty on λ_c is

$$(\sigma_{\lambda})^2 = (\sigma_{\lambda}^{\text{stat}})^2 + (\sigma_{\lambda}^{\text{cal}})^2. \quad (8)$$

The composition of the final wavelength error budget is detailed in Section 3.6.1.

The realized laser wavelength is never the one a priori asked for, as shown in Figures 9 and 14. However, we observed remarkable repeatability of the correspondence between the set wavelength λ_L and the realized wavelength λ_c in Figure 14. This figure represents every $\approx 350\,000$ laser bursts shot and analyzed during the CBP measurement campaign. The superimposition of all measurements at each laser wavelength λ_L exhibits good laser stability with time and of the λ_c wavelength fit with line intensity. The RMS is better than 0.02 nm at most wavelengths, except where line determination is ambiguous: close to the contamination lines at 532 nm and 1064 nm, and close to the sensor edges. Given this remarkable stability, to improve the line detection in

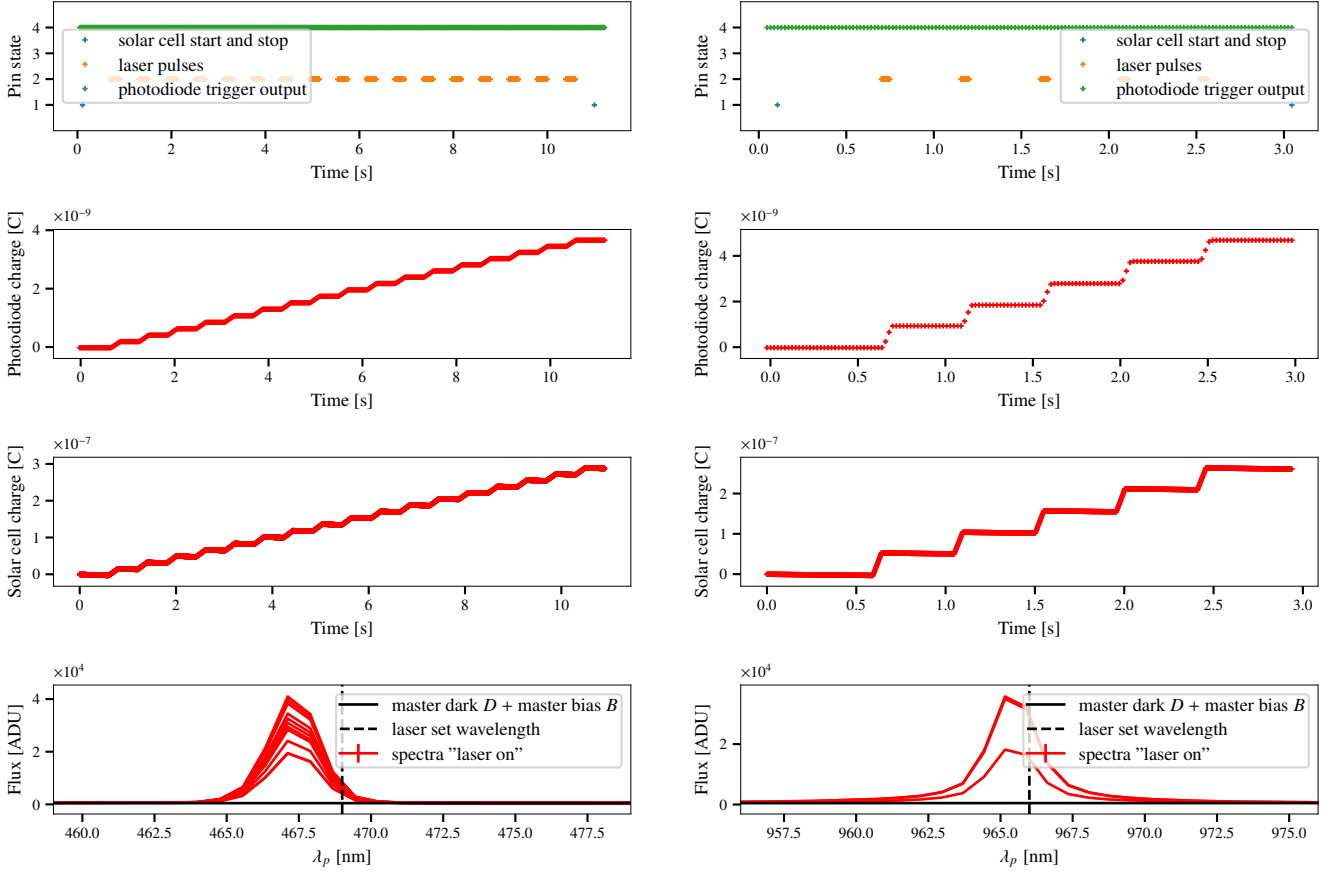


Fig. 9: Data set examples when targeting the solar cell. From top to bottom: typical data sets for digital analyzer (pin state 4 is the Keithley output, pin state 2 the laser trigger output, pin state 1 the Keysight start and end time acquisition time stamps), charges in the photodiode, charges in the solar cell, flux in the spectrograph. Left: typical data set at 469 nm. Right: typical data set at 966 nm.

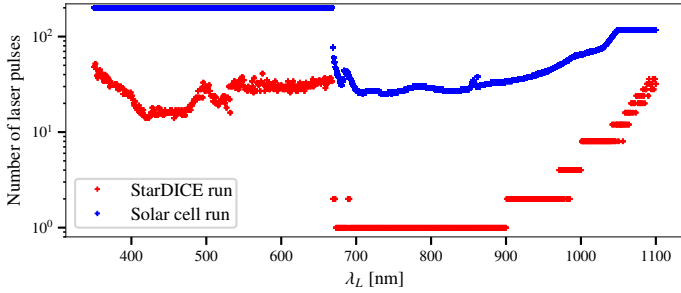


Fig. 10: Number of laser pulses per burst used for solar cell and StarDICE runs.

weak laser regimes (like below 400 nm), we averaged the obtained λ_c for each λ_L . We decided to use this average as our final calibrated wavelength (black curve in Figure 14). As the bijection between λ_L laser wavelengths and realized wavelengths λ_c is unambiguous, in some figures of this paper, we use the set laser wavelength λ_L for clarity.

3.3.4. Light contamination measurements

In addition to using the spectrograph to monitor the wavelength of the laser lines, we also used it in a spectro-photometric mode to estimate light contamination.

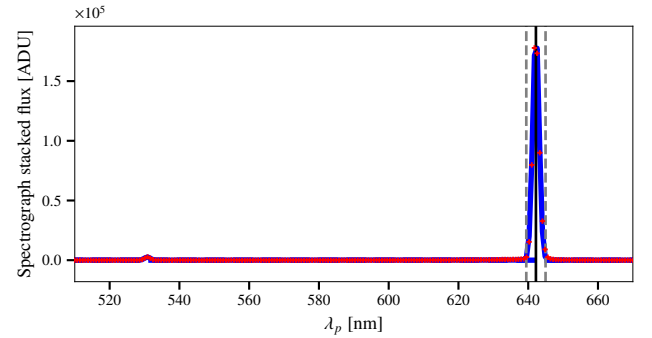


Fig. 11: Fit of Gaussian profiles (blue lines) in the stacked spectra (red dots) for a laser line set at $\lambda_L = 643$ nm, with raw spectrograph wavelengths on the abscissa axis. The contamination line at 532 nm is also visible. The black vertical line gives the fitted laser line centroid. The grey vertical lines delimit a region of $\pm 3\sigma_g$ around the centroid, where σ_g is the fitted RMS of the Gaussian profile. The total laser flux is the sum of the pixel values in this region.

The secondary laser lines at 532 nm and from two-photon conversions were our principal suspects of internal laser light contamination. Indeed, we noticed the presence of a 532 nm line

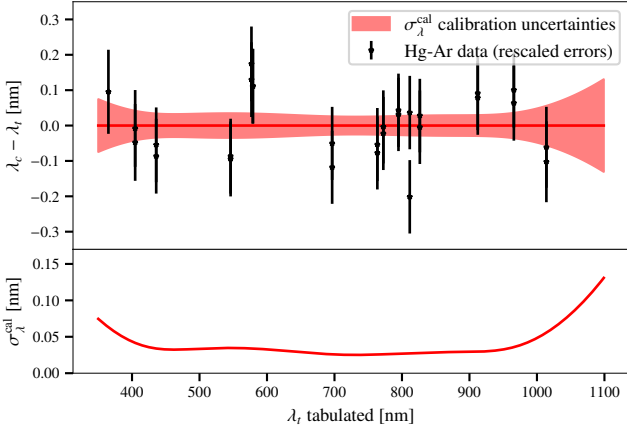


Fig. 12: Spectrograph calibration plot. Top: difference between the tabulated Hg-Ar emission line wavelengths λ_l and the wavelengths computed using the spectrograph calibration function $c(\lambda_g)$. Data taken before and after the data acquisition campaign are superimposed. Their uncertainties were re-scaled with a common factor to get a final reduced χ^2 of one. The red band represents the systematic uncertainty band from the $c(\lambda_g)$ fit on data with the uncertainty rescaling. Bottom: emphasis on the systematic uncertainties of the spectrograph calibration procedure.

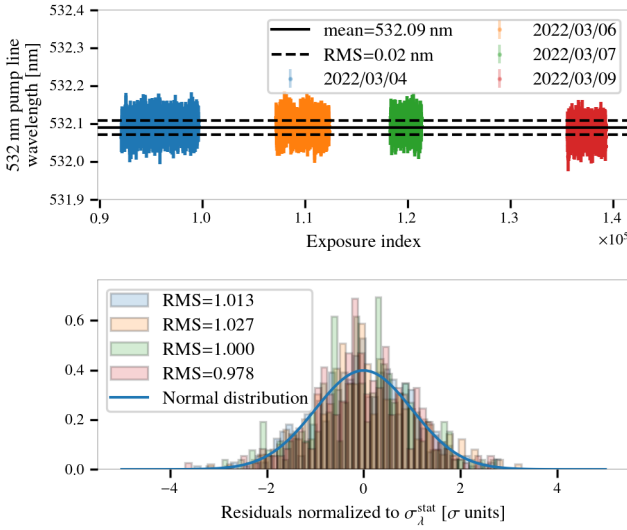


Fig. 13: Top: all measured 532 nm pump line calibrated wavelengths with respect to exposure index ($\approx 250\,000$ data points) for the four solar cell runs. Bottom: distributions of residuals to the mean wavelength normalized by $\sigma_{\lambda}^{\text{stat}}$ (colored bars) with RMS quoted in legend. A normal distribution of RMS 1 is over-plotted for comparison.

in the regime 532 to 669 nm and of a weak line when the laser is set to wavelength above 1064 nm. For the latter, if we call λ_L the wavelength at which the laser was set, we observed the production of photons at wavelength λ_{comp} , which seems given by

$$\frac{2}{1064 \text{ nm}} \approx \frac{1}{\lambda_L} + \frac{1}{\lambda_{\text{comp}}} \quad (9)$$

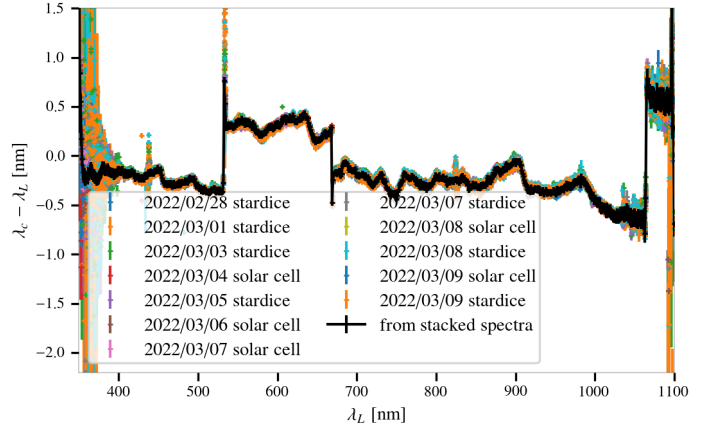


Fig. 14: Difference between the calibrated λ_c and requested laser wavelengths λ_L , for all the $\approx 350\,000$ laser line wavelengths acquired during our measurement campaign.

due to the conversion of two 1064 nm photons into a laser photon at λ_L and a complementary photon at λ_{comp} that ended in the laser beam. In practice, we observed a small emission line in the spectrograph when $\lambda_L > 1064$ nm, nearly symmetrical of the laser line with respect to 1064 nm.

The laser line flux $Q_{\text{spectro}}^{\text{main}}$, the 532 nm line flux Q_{spectro}^{532} and the λ_{comp} line flux $Q_{\text{spectro}}^{\text{comp}}$ flux are computed summing the pixels in a window of $\pm 3\sigma_g$, after dark and bias subtraction. Associated statistical uncertainties are computed from the standard error propagation of the $\sigma_{i,p}$ values. These fluxes are used to correct solar cell and photodiode charges as well as the StarDICE photometry from the 532 nm line contamination (see Section 3.6.3).

Finally, we needed to build an error model of the measured spectrograph fluxes to measure the level of contamination from photons not belonging to the main laser line. We used the dark exposures acquired with different exposure times to estimate it.

The master bias was subtracted from all dark exposures. We measured the readout noise and sensor gain from those data by doing the following procedure. Let's call $D(\lambda_p)$ the dark exposure minus the master bias value for pixel p . For each exposure time, the variance σ_p^2 and average $\bar{D}(\lambda_p)$ of each $D(\lambda_p)$ pixel were computed. The variance evolution with the average is well described by a second-order polynomial function, parameterized as follows:

$$\sigma_p^2 = \sigma_{ro}^2 + \bar{D}(\lambda_p)/G + \sigma_G^2 \bar{D}^2(\lambda_p)/G^2 \quad (10)$$

with σ_{ro} the readout noise, G the sensor gain and σ_G a statistical noise on the gain itself. The fit of this model to data led to the following values (Figure 15):

$$\sigma_{ro} = 1.26 \text{ ADU}, \quad (11)$$

$$G = 25.8 \text{ e}^-/\text{ADU}, \quad (12)$$

$$\sigma_G/G = 0.7\%. \quad (13)$$

The first two values are compatible with the sensor specifications given by the spectrograph vendor³. With this error model, error bars are compatible with the observed dispersion in the dark parts of the spectra.

³ For the QE65000 fiber spectrograph, the vendor specifies a read-out noise of 1.5 ADU (or 40 electrons) and thus a gain of 26 e^-/ADU .

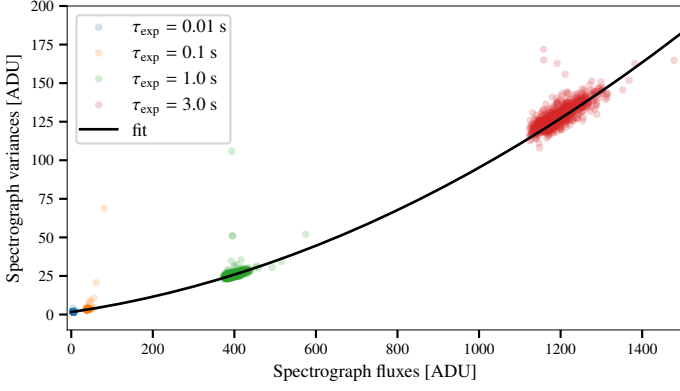


Fig. 15: Spectrograph photon transfer curve to estimate gain and read-out noise. Pixel variance from dark spectra is represented versus their averages for four different exposure times τ_{exp} .

3.4. Electrometer data reduction

In one data set, we accumulated several laser bursts, and a per-burst analysis was conducted to be able to remove outliers more easily. All bursts are combined only at the end of the analysis to get the CBP and StarDICE responses.

3.4.1. Photodiode data reduction

Photodiode data are charge time series with stair-case shape. Each step is a laser burst, and the step height roughly gives the charge $Q_{\text{phot}}^{\text{mes}}$ accumulated during a laser burst (see Figures 9 and 16). The length of the charge rise is the laser burst duration τ_b while flat sequences are dark times. For the photodiode, the time stamps come directly from the digital analyzer clock, with a sampling at 50 Hz. The digital analyzer clock also provides the time stamps of the laser pulses.

For each burst, we fit straight (almost horizontal) lines in the charge sequence during the dark times before and after a laser burst, removing the closest points to the burst. During those intervals, the charge evolution measures the charge leak corresponding to the dark current we need to account for.

We call t_1 and t_2 the time stamps of the beginning and end of the laser burst, respectively, given by the laser trigger output itself. The accumulated charge $Q_{\text{phot}}^{\text{mes}}$ during a burst is then

$$q_{\text{phot}}^{\text{dark}}(t) = a_{\text{phot}}t + b_{\text{phot}} \quad (14)$$

$$Q_{\text{phot}}^{\text{mes}} = q_{\text{phot},2}^{\text{dark}}(t_2) - q_{\text{phot},1}^{\text{dark}}(t_1) - \frac{1}{2} \left[q_{\text{phot},1}^{\text{dark}}(t_2) - q_{\text{phot},1}^{\text{dark}}(t_1) + q_{\text{phot},2}^{\text{dark}}(t_2) - q_{\text{phot},2}^{\text{dark}}(t_1) \right] \quad (15)$$

where $q_{\text{phot},j}^{\text{dark}}(t_i)$ is the line fit of the dark part j ($j = 1$ before the burst, $j = 2$ after) evaluated at time t_i . The term in brackets subtracts an estimation of the dark current contribution during the burst itself. After this procedure, the subtraction $q_{\text{phot},2}^{\text{dark}}(t_2) - q_{\text{phot},1}^{\text{dark}}(t_1)$ gives the raw height of the burst step in the charge sequence⁴ while the terms in brackets remove the averaged contribution of the dark current using both dark times before and after the burst. Note that we do not model anything during the burst time, as the laser power stability does not guarantee

⁴ Moreover, doing the subtraction removes systematic inaccuracy coming from the Keithley electrometer.

that this can be modeled with a simple mathematical function. The only model assumption is that dark sequences are modeled with straight lines.

The fit of the two parameters a_{phot} and b_{phot} of each $q_{\text{phot},j}^{\text{dark}}(t)$ line models is performed via a standard χ^2 minimization, using the `curve_fit` method from python library `scipy`. Uncertainties on the data points, equally weighted, are tuned so that the final reduced χ^2 is one. As a result, we assume that the fit residuals are only due to Gaussian instrumental noise, as justified by Figure 16. The analysis of the residuals also confirms our choice to use order 1 polynomial functions to model the dark sequences.

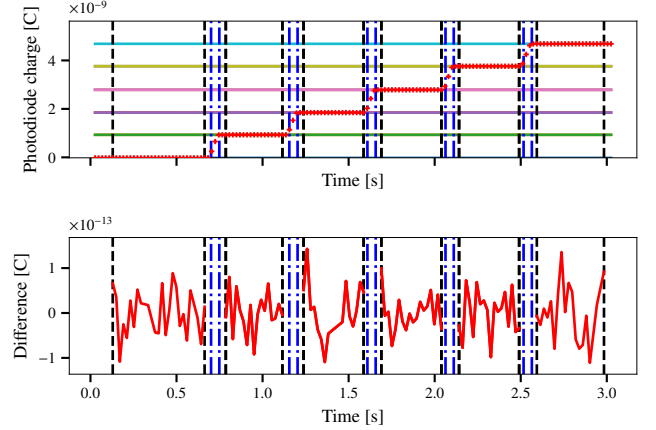


Fig. 16: Photodiode charge sequence reduction process at wavelength $\lambda_L = 469$ nm. Vertical blue lines indicate the laser starts and stops, while black lines flank the dark sequences. Colored horizontal lines are fitted during dark times. The top panel shows the raw charges acquired with the photodiode, while the bottom panel shows the residuals of the linear fits during dark times.

Covariance matrix uncertainties from all linear model parameters are then propagated to compute the statistical uncertainty $\sigma_{\text{phot}}^{\text{stat}}$ of $Q_{\text{phot}}^{\text{mes}}$ per burst. They are typically of the order of the residual RMS, around 5×10^{-5} nC (Figure 16), more than three orders of magnitude below the typical $Q_{\text{phot}}^{\text{mes}}$ values. We tested the fitting procedure on pure dark sequences and found an unbiased null measurement $Q_{\text{phot}}^{\text{dark}}$ with a pull distribution of RMS ≈ 1 whatever the burst duration τ_b ; computed statistical uncertainties $\sigma_{\text{phot}}^{\text{stat}}$ nicely covers the data Gaussian noise (Figure 17).

3.4.2. Solar cell data reduction

Solar cell charge time series are very similar to photodiode time series (see Figures 9 and 18). However, they are affected by two supplementary contributions as seen in the noise power spectrum: a random $1/f$ noise and power line harmonics mainly at 50 Hz and 100 Hz (Figure 6). Time-stamps come directly from the Keysight electrometer. However, as this device sends triggers at the start and end of the acquisition, the electrometer clock is re-scaled using the digital analyzer. In doing so, all electrometers are synchronized via the digital analyzer's internal clock.

As for the photodiode, we modeled the dark current by estimating the charge decrease over the regions before and after each laser burst by fitting the slope of their departure from horizontal. The solar cell dark model is the sum of a linear function plus two

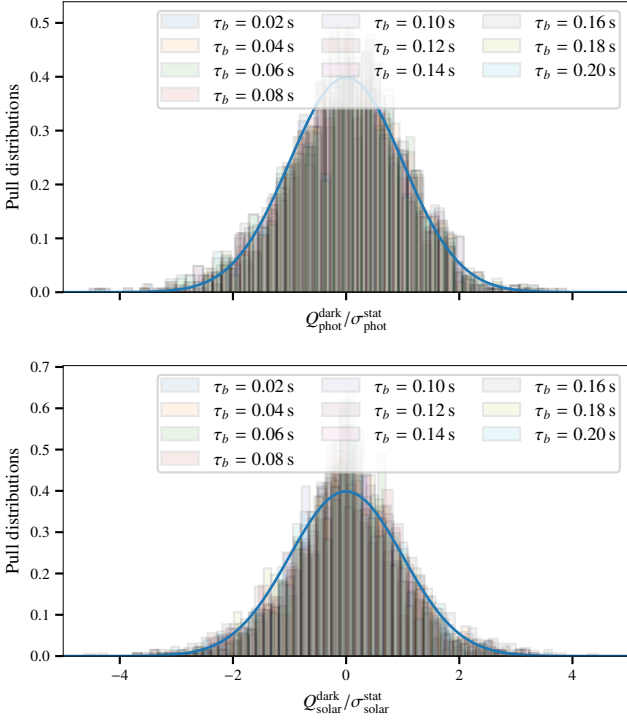


Fig. 17: Top: pull distributions for photodiode charge measurements during pure dark time series $Q_{\text{phot}}^{\text{dark}}/\sigma_{\text{phot}}^{\text{stat}}$, with different burst durations τ_b . The cyan curve represents a Gaussian distribution of mean 0 and RMS 1. Bottom: same but for the solar cell case $Q_{\text{solar}}^{\text{dark}}/\sigma_{\text{solar}}^{\text{stat}}$.

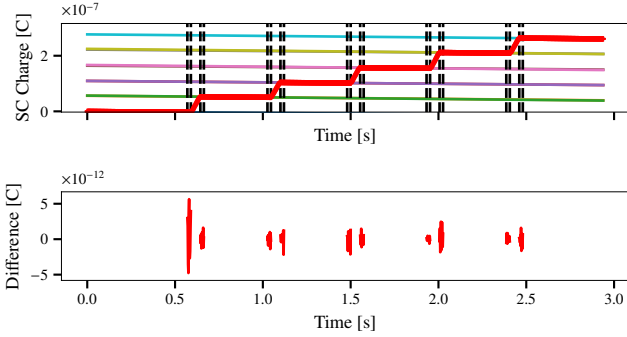


Fig. 18: Solar cell charge sequence reduction process at wavelength $\lambda_L = 469$ nm. Pairs of vertical black at the left and right of a burst encompass the fitted dark sequences. Colored curves are the dark model fitted within these dark times. The top panel shows the raw charges acquired with the solar cell, while the bottom panel shows the residuals to the dark model fit during dark times only.

sinusoidal functions at fixed frequency 50 Hz and 100 Hz:

$$q_{\text{solar}}^{\text{dark}}(t) = a_{\text{solar}}t + b_{\text{solar}} + A_{50} \sin(100\pi t + \phi_{50}) + A_{100} \sin(200\pi t + \phi_{100}) \quad (16)$$

where a_{solar} , b_{solar} , A_{50} , A_{100} , ϕ_{50} and ϕ_{100} are free parameters fitted on data. Again, we call t_1 and t_2 the time stamps of the beginning and end of the laser burst, respectively, given by the

laser trigger output itself. The accumulated charge $Q_{\text{solar}}^{\text{mes}}$ during a burst is then

$$Q_{\text{solar}}^{\text{mes}} = q_{\text{solar},2}^{\text{dark}}(t_2) - q_{\text{solar},1}^{\text{dark}}(t_1) - \frac{1}{2} \left[q_{\text{solar},1}^{\text{dark}}(t_2) - q_{\text{solar},1}^{\text{dark}}(t_1) + q_{\text{solar},2}^{\text{dark}}(t_2) - q_{\text{solar},2}^{\text{dark}}(t_1) \right] \quad (17)$$

where the indices 1 and 2 refer again to data before and after the burst, respectively. Free $q_{\text{solar}}^{\text{dark}}(t)$ parameters were fitted, minimizing a χ^2 with a Newton-Raphson gradient descent. Power lines are well fitted by the model (no more periodic oscillations in the residuals) as shown in Figure 19 where A_{50} was about 50 pC. The $1/f$ noise is not modeled in $q_{\text{solar}}^{\text{dark}}(t)$ as it is sub-dominant, but the lowest frequency modes are captured by the values of a_{solar} and b_{solar} . To get a close estimate of their contributions during the burst, we fit the dark sequences only during $\tau_b/2$ around the burst to rely on their extrapolation inside the burst window (with a minimum of 12 data points to encompass at least one 50 Hz period). Indeed, as exhibited in Figure 19, fits of $q_{\text{solar},2}^{\text{dark}}(t)$ after the first burst (orange) and of $q_{\text{solar},1}^{\text{dark}}(t)$ before the second burst (green) do not superimpose because of the departure from linearity due to the long-range $1/f$ noise. So restricting the fits in two windows of size $\max(22 \text{ ms}, \tau_b/2)$ permits to capture contaminating $1/f$ modes no longer than τ_b .

The charge value $Q_{\text{solar}}^{\text{mes}}$ is computed for each laser burst following Equation 17. Concerning estimating its statistical uncertainties $\sigma_{\text{solar}}^{\text{stat}}$, we add in quadrature the contributions from the parameter covariance matrix and the RMS of the residuals (to account for uncaptured $1/f$ modes). We trained the fitting procedure on pure dark data and noticed that $\sigma_{\text{solar}}^{\text{stat}}$ was too small to account for $Q_{\text{solar}}^{\text{dark}}$ null measurement dispersion. The RMS of the pull distributions was linearly dependent on the burst duration τ_b , showing $\sigma_{\text{solar}}^{\text{stat}}$ did not capture all the long-range $1/f$ noise. Therefore, we corrected all $\sigma_{\text{solar}}^{\text{stat}}$ values with a multiplicative factor dependent on τ_b . Doing so, we found an unbiased null measurement $Q_{\text{solar}}^{\text{dark}}$ with a pull distribution of RMS ≈ 1 whatever the burst duration τ_b (Figure 17).

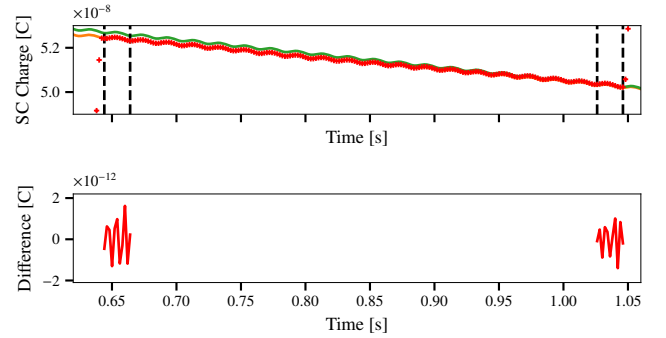


Fig. 19: Same as Figure 18 but zoomed on the second dark sequence. The orange model is fitted on dark data on the left of the plot, while the green model is fitted on dark data on the right.

3.5. CBP ratio of charges

The ratio of charges $r_{\text{CBP}}^{\text{mes}} = Q_{\text{solar}}^{\text{mes}}/Q_{\text{phot}}^{\text{mes}}$ is computed to check the statistical uncertainties and then analyze systematic uncertainties. It is presented in Figure 20. Each black point is a ratio of charge measurements from one burst at one wavelength λ_L .

They follow a smooth curve in λ_L . The $r_{\text{CBP}}^{\text{mes}}$ statistical uncertainties

$$\sigma_{\text{CBP}}^{\text{stat}} = r_{\text{CBP}}^{\text{mes}} \sqrt{\left(\frac{\sigma_{\text{solar}}^{\text{stat}}}{Q_{\text{solar}}^{\text{mes}}}\right)^2 + \left(\frac{\sigma_{\text{phot}}^{\text{stat}}}{Q_{\text{phot}}^{\text{mes}}}\right)^2} \quad (18)$$

are higher in the blue as the laser is weaker in this regime (around 0.1%) than in the red (around 0.01%). They were estimated as the difference between all data points and a spline interpolation, normalized by the statistical uncertainties. As expected, they follow a Gaussian distribution of mean 0 and RMS ≈ 1 .

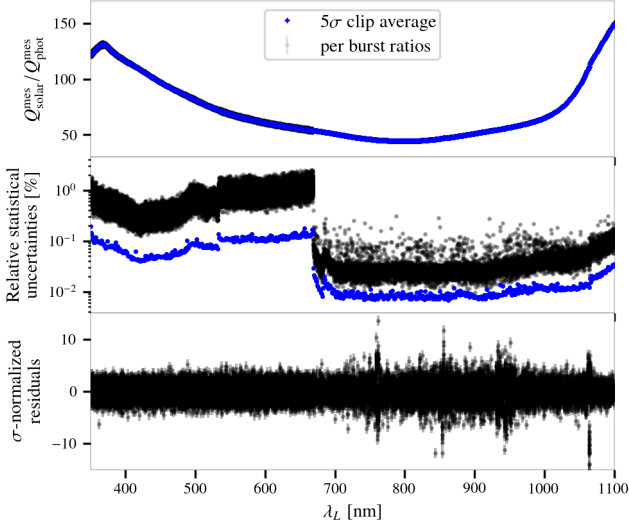


Fig. 20: CBP charge ratio $Q_{\text{solar}}^{\text{mes}}/Q_{\text{phot}}^{\text{mes}}$ as a function of λ_L . Top: every black point is a charge measurement ratio from one burst, and the blue curve is the 5σ -clipped average. Middle: relative uncertainties on $Q_{\text{solar}}^{\text{mes}}/Q_{\text{phot}}^{\text{mes}}$. Bottom: pull distribution after spline subtraction.

3.6. Systematics

3.6.1. Wavelength calibration

Figure 21 details the total error budget from wavelength calibration for three different runs: two runs shooting at StarDICE with two pinholes and one run shooting at the solar cell. Uncertainty on wavelength σ_{λ} is primarily dominated by wavelength calibration uncertainties in the range 400 to 1080 nm. Statistical uncertainty dominates around 532 nm and close to the spectrograph sensor edges. Except in these cases, σ_{λ} is well below 0.1 nm. There are no noticeable differences despite the different experimental conditions for the three runs presented in Figure 21.

To evaluate the systematic uncertainty on the CBP response due to the wavelength calibration, we computed r_{CBP} at $\lambda_c + \sigma_{\lambda}^{\text{cal}}$ and $\lambda_c - \sigma_{\lambda}^{\text{cal}}$. The difference between both CBP responses is well below the statistical uncertainty since the CBP response varies slowly in λ (Figure 20) and the whole $\sigma_{\lambda} < 0.1$ nm (Figure 21). The wavelength measurement uncertainty has a systematic effect mainly in determining the sharp edges of the filter pass-bands.

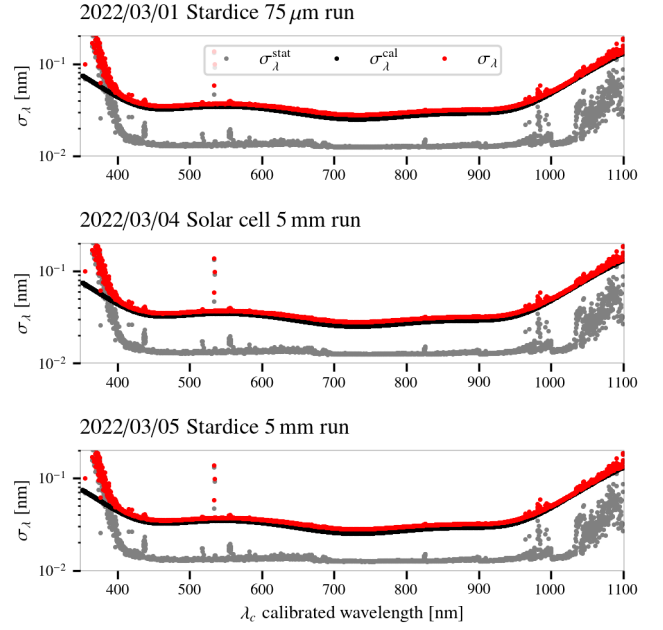


Fig. 21: Total error budget (red) of calibrated wavelengths λ_c for three different runs (from top to bottom: StarDICE run with 75 μm pinhole, solar cell run with 5 mm pinhole, StarDICE run with 5 mm pinhole) as a function of the laser set wavelength λ_L . Detection uncertainties (grey) represent PSF modeling uncertainties and Gaussian fit uncertainties, while calibration uncertainties (black) come from the Hg-Ar lamp calibration procedure.

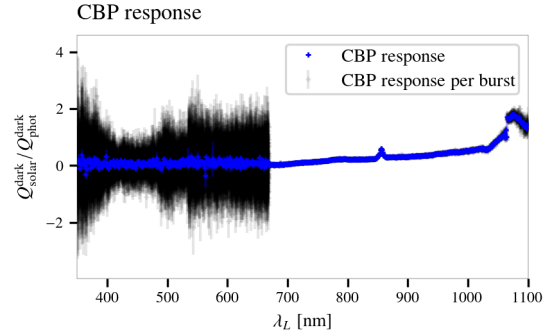


Fig. 22: CBP charge ratio $Q_{\text{solar}}^{\text{dark}}/Q_{\text{phot}}^{\text{dark}}$ as a function of λ_L : every black point is a charge measurement ratio from one burst, the blue curve is the 5σ -clipped average.

3.6.2. Ambient light

We ran a solar cell acquisition with a cap on the CBP telescope to measure the ambient light contamination. This setup mimics a regular solar cell acquisition without direct light, therefore specifically measuring the laser light leaks during operation. The measurement of this indirect ambient light $Q_{\text{solar}}^{\text{dark}}$ constitutes a "dark" for our CBP calibration. From this specific run, we built a dark CBP response $r_{\text{CBP}}^{\text{dark}} = Q_{\text{solar}}^{\text{dark}}/Q_{\text{phot}}^{\text{dark}}$ where $Q_{\text{solar}}^{\text{dark}}$ (resp. $Q_{\text{phot}}^{\text{dark}}$) is the burst charge collected in the solar cell (resp. the photodiode). For each λ_L , burst ratios are averaged with a 5σ clipping, giving the blue curve $r_{\text{CBP}}^{\text{dark}}(\lambda_L)$ in Figure 22. The high dispersion

below 670 nm corresponds to the wavelength regime where the laser power is low, inducing a faint ambient light poorly measured. The dark contribution in our solar cell data is then evaluated as follows:

$$Q_{\text{solar}}^{\text{dark}} = r_{\text{CBP}}^{\text{dark}}(\lambda_L) \times Q_{\text{phot}}^{\text{mes}}(\lambda_L) \quad (19)$$

and subtracted from all our measurements. This correction is the main contribution to instrumental non-linearity we identified.

3.6.3. Laser light contamination

As described in Section 2.2, the light source used is a tunable laser using a pump laser at 532 nm, which has different regimes. When we operated within the range [532 - 644] nm, we detected in the spectrograph a contamination light at 532 nm for all wavelengths in this range.

We must account for this light contamination to get the true amount of charges $Q_{\text{solar}}^{\text{cal}}$ coming from the main laser line. We built a model for the 532 nm contribution observed in the range [532 - 644] nm. The total charge measured in the solar cell $Q_{\text{solar}}^{\text{mes}}$ is the sum of the charges from the main wavelength λ_L and the charges from contaminations, like the 532 nm contamination. The same applies to the total charges measured in the photodiode $Q_{\text{phot}}^{\text{mes}}$ with Q_{phot} and Q_{phot}^{532} respectively, the charges from the main laser line and the charges from the 532 nm contamination:

$$Q_{\text{phot}}^{\text{mes}}(\lambda_L) = Q_{\text{phot}}(\lambda_L) + Q_{\text{phot}}^{532}(\lambda_L) \quad (20)$$

In the spectrograph, we measured two fluxes from two separated peaks: the one from the main wavelength $Q_{\text{spectro}}^{\text{main}}$, and the one from the 532 nm contamination Q_{spectro}^{532} . As the light is homogeneous in the integrating sphere, the proportion of contamination light and laser light is the same for both instruments. This translates into:

$$\frac{Q_{\text{spectro}}^{532}}{Q_{\text{spectro}}^{\text{main}}} \times \frac{\epsilon_{\text{spectro}}(\lambda_L)}{\epsilon_{\text{spectro}}(532)} = \frac{Q_{\text{phot}}^{532}}{Q_{\text{phot}}^{\text{main}}} \times \frac{\epsilon_{\text{phot}}(\lambda_L)}{\epsilon_{\text{phot}}(532)} \quad (21)$$

where $\epsilon_{\text{phot}}(\lambda_L)$ and $\epsilon_{\text{spectro}}(\lambda_L)$ are the quantum efficiencies of the photodiode and the spectrograph sensor with its optical fiber, respectively. The ratio:

$$\eta(\lambda) = \frac{\epsilon_{\text{spectro}}(\lambda)}{\epsilon_{\text{phot}}(\lambda)} = \frac{Q_{\text{spectro}}^{\text{main}}(\lambda)}{Q_{\text{phot}}^{\text{main}}(\lambda)} \quad (22)$$

can be obtained either as a dimensionless quantity from the manufacturer data sheets (Figure 23) or directly measured in spectrograph ADU per photodiode unit (Figure 23). In the following, we used the spline interpolation of the measured ratio and quoted as uncertainty the RMS of the resulting residuals.

We denote the level of contamination in the photodiode $Q_{\text{phot}}^{\lambda_L}/Q_{\text{phot}}^{532}$ by the ratio $\alpha(\lambda)$ that reads:

$$\alpha(\lambda_L) = \frac{Q_{\text{phot}}^{532}(\lambda_L)}{Q_{\text{phot}}(\lambda_L)} = \frac{Q_{\text{spectro}}^{532}(\lambda_L)}{Q_{\text{spectro}}^{\text{main}}(\lambda_L)} \times \frac{\epsilon_{\text{spectro}}(\lambda_L)\epsilon_{\text{phot}}(532)}{\epsilon_{\text{phot}}(\lambda_L)\epsilon_{\text{spectro}}(532)} \quad (23)$$

We measured $\alpha(\lambda_L)$ at every wavelength using the spectrograph fluxes for the main line and the 532 nm contaminant (Figure 24). We rejected data where $\sigma_{\lambda} > 0.1$ nm to remove instances where the main line and the 532 nm contaminant are poorly separated. In the 532 - 540 nm range, where an unambiguous separation between the main line and the contaminant proved infeasible, we extrapolated the Q_{spectro}^{532} values by a linear interpolation

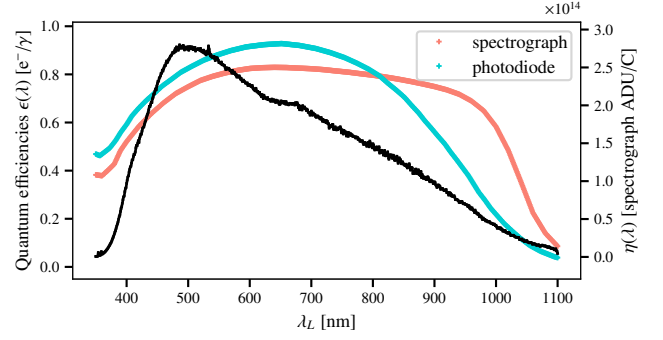


Fig. 23: Quantum efficiencies of the spectrograph (red) and the photodiode (cyan), with the $\eta(\lambda)$ ratio (black).

over the entire range where Q_{spectro}^{532} was available. The resulting $\alpha(\lambda_L)$ yield a rather flat curve between 540 and 644 nm with small wiggles around a global slope of $\sim 1\%$. Uncertainties are propagated in the extrapolation range using the standard error propagation formula, considering the covariances between the 2 model parameters. With this α model, we deduced the true photodiode charges coming from the main laser line at λ_L

$$Q_{\text{phot}}^{\text{cal}}(\lambda_L) \equiv \frac{Q_{\text{phot}}^{\text{mes}}(\lambda_L)}{1 + \alpha(\lambda_L)} \quad \text{if } \lambda_L \in [532, 644] \text{ nm} \quad (24)$$

We introduce here the notation $Q_{\text{phot}}^{\text{cal}}$ as the final calibrated amount of charges detected in the photodiode per laser burst.

Light detected by the solar cell has gone through the CBP optics, with a response R_{CBP} . Then, the contribution of the 532 nm photons collected by the solar cell is computed as

$$\begin{aligned} Q_{\text{solar}}^{532}(\lambda_L) &= R_{\text{CBP}}(532)Q_{\text{phot}}^{532}(\lambda_L) \\ &= R_{\text{CBP}}(532) \frac{\alpha(\lambda_L)}{1 + \alpha(\lambda_L)} Q_{\text{phot}}^{\text{mes}}(\lambda_L). \end{aligned} \quad (25)$$

Thanks to the spectrograph data, using Equations 24 and 25, we can correct all our measurements from the 532 nm in both the photodiode and the solar cell. The impact of this correction is illustrated in Section 3.6.8.

We did the same correction for the complementary wavelength line λ_{comp} appearing after $\lambda_L > 1064$ nm. The correction coefficient β analogue to α is

$$\beta(\lambda_L) = \frac{Q_{\text{phot}}^{\lambda_{\text{comp}}}(\lambda_L)}{Q_{\text{phot}}(\lambda_L)} = \frac{Q_{\text{spectro}}^{\lambda_{\text{comp}}}(\lambda_L)}{Q_{\text{spectro}}^{\text{main}}(\lambda_L)} \times \frac{\epsilon_{\text{spectro}}(\lambda_L)\epsilon_{\text{phot, comp}}}{\epsilon_{\text{phot}}(\lambda_L)\epsilon_{\text{spectro, comp}}} \quad (26)$$

and is represented Figure 25. The $Q_{\text{spectro}}^{\lambda_{\text{comp}}}$ data points were modeled by a linear function to allow extrapolating β in the range [1064 - 1070] nm. Similarly, the calibrated amount of charges in the photodiode corrected from the λ_{comp} photons is

$$Q_{\text{phot}}^{\text{cal}}(\lambda_L) \equiv \frac{Q_{\text{phot}}^{\text{mes}}(\lambda_L)}{1 + \beta(\lambda_L)} \quad \text{if } \lambda_L > 1064 \text{ nm} \quad (27)$$

and their contribution $Q_{\text{solar}}^{\lambda_{\text{comp}}}$ in the solar cell is given by

$$\begin{aligned} Q_{\text{solar}}^{\lambda_{\text{comp}}}(\lambda_L) &= R_{\text{CBP}}(\lambda_{\text{comp}})Q_{\text{phot}}^{\lambda_{\text{comp}}}(\lambda_L) \\ &= R_{\text{CBP}}(\lambda_{\text{comp}}) \frac{\beta(\lambda_L)}{1 + \beta(\lambda_L)} Q_{\text{phot}}^{\text{mes}}(\lambda_L). \end{aligned} \quad (28)$$

Both corrections' impact are illustrated in Section 3.6.5 and Figure 27, and Section 4.2.

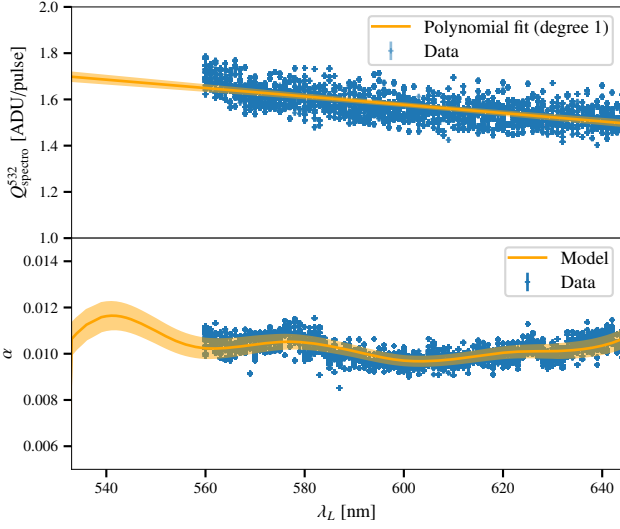


Fig. 24: Top: all available data points for α computed from the spectrograph measurements (blue crosses) and linear fit (orange) with its uncertainty (shaded orange band). Bottom: difference between data and model.

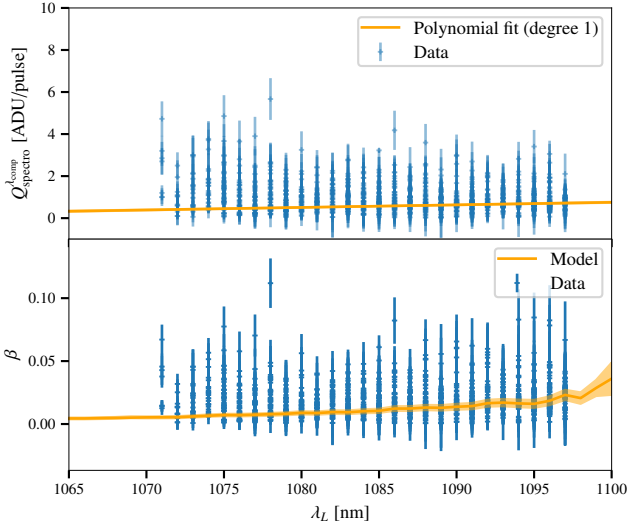


Fig. 25: Same as Figure 24 but for β correction coefficient.

3.6.4. Integrating sphere fluorescence

Our integrating sphere appeared to be fluorescent at laser wavelengths below 400 nm. The fluorescence of integrating spheres is studied in Shaw et al. (2007). The fluorescent signal is visible in the StarDICE camera using the g filter or the grating but is very weak in the spectrograph. To visualize and model it, we stacked all our spectra in bins of 5 nm in λ_L (Figure 26 top). The fluorescence signal spans a range of wavelength between ≈ 400 nm and ≈ 500 nm, with an emission peak around 450 nm.

To estimate the contamination from fluorescence photons, we fitted a fluorescence spectrum model taken from Figure 9 of Shaw et al. (2007), with a constant background and a Moffat profile for the laser line for each stacked spectra. The fluorescence spectrograph flux is converted into photodiode charges $Q_{\text{phot}}^{\text{fluo}}$ us-

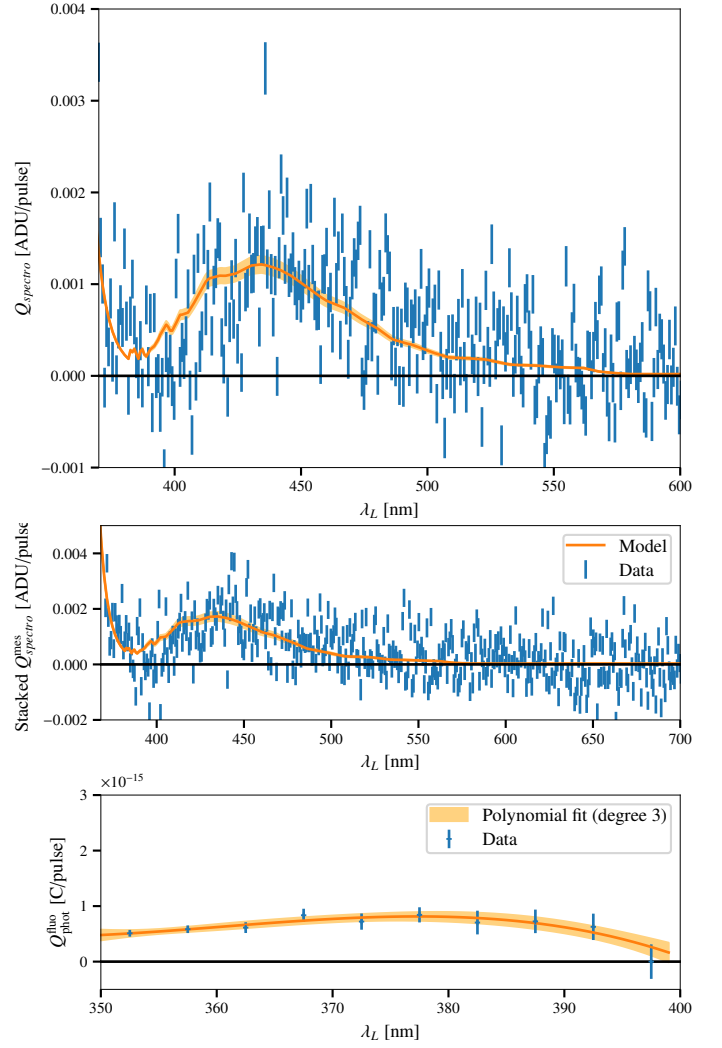


Fig. 26: Top: integrating sphere fluorescence spectrum from a stack of all solar cell run data with $\lambda_L < 370$ nm (blue crosses), with the best-fit model (orange line). Bottom: estimated fluorescence contribution in photodiode measured charges $Q_{\text{phot}}^{\text{fluo}}$ as a function of wavelength (blue crosses) with a fitted third-order polynomial function (orange line).

ing the $\eta(\lambda)$ conversion factor and normalized by the total number of laser pulses (Figure 26 bottom)⁵. We observed that the fluorescence spectrum cancels at $\lambda_L \geq 400$ nm. For every wavelength $\lambda_L < 400$ nm, we evaluate and subtract the contribution from the fluorescence contamination in the photodiode using the $Q_{\text{phot}}^{\text{fluo}}(\lambda_L)$ model from Figure 26:

$$Q_{\text{phot}}^{\text{cal}}(\lambda_L) \equiv Q_{\text{phot}}^{\text{mes}}(\lambda_L) - Q_{\text{phot}}^{\text{fluo}}(\lambda_L) \quad \text{if } \lambda_L < 400 \text{ nm} \quad (29)$$

We perform identically for $Q_{\text{solar}}^{\text{mes}}$ multiplying by the CBP response at 450 nm:

$$Q_{\text{solar}}^{\text{fluo}}(\lambda_L) = R_{\text{CBP}}(450)Q_{\text{phot}}^{\text{fluo}}(\lambda_L) \quad (30)$$

This correction's impact is illustrated later in Section 4.2.

After the fluorescence, 532 nm and λ_{comp} corrections, we updated our $\eta(\lambda)$ estimate and iterated several times to refine the light contamination subtractions.

⁵ Contrary to the 532 nm line contamination correction, we can not normalize by the flux in the main laser line as it is often noise-dominated in un-stacked spectra when $\lambda_L < 400$ nm.

3.6.5. Instrumental chain linearity check

For the two solar cell runs we undertook, we varied the laser output power by a factor of around 2, namely QSW at maximum and QSW set at 298. The ratio of the two CBP charge ratios before and after dark subtraction is presented in Figure 27. No corrections lead to a ≈ 5 permil deviations of the two CBP responses with respect to wavelength. Both CBP responses agree at ≈ 0.5 permil for wavelengths above 669 nm when applying dark subtraction. Then, laser contamination correction makes the two CBP responses agree in the [532, 669] nm range better than 0.1 permil.

To assess the value of systematic uncertainties on the CBP response due to non-linearities, we take the absolute distance of the binned ratio to unity in four different ranges of wavelengths after dark subtraction and laser contamination correction (red segments in the bottom plot of Figure 27).

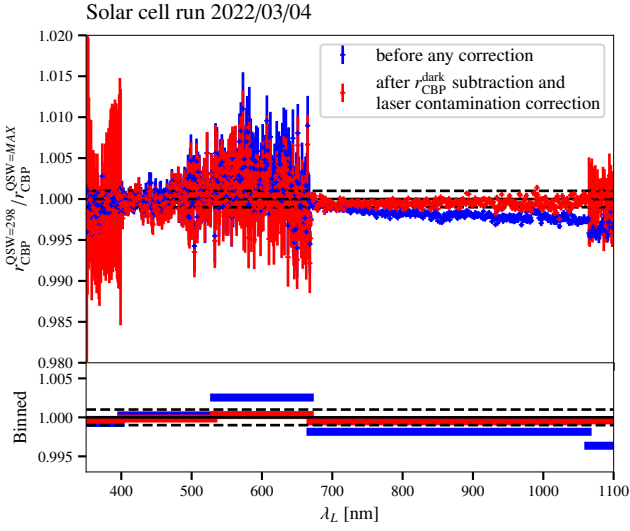


Fig. 27: Ratios of the CBP charge ratio for two different QSW values as a function of λ_L coming from the 2022/03/04 solar cell run. Blue is for raw data, while red is used for data corrected by dark contribution and laser contaminations. Black dashed lines encompass the permil precision region. Top: ratios for each λ_L . Bottom: binned ratio for four different wavelength ranges. A similar plot is obtained for the 2022/03/06 solar cell run.

3.6.6. CBP scattered light varying the solar cell distance

To measure the influence of scattered light in the CBP beam, we measured the CBP throughput by putting the solar cell 16 cm farther and compared it to the initial value. At this new position, we measured again the CBP dark from solar cell $Q_{\text{solar}}^{\text{dark}}$. Dark subtraction and laser contamination correction are applied. The comparison of both transmissions is presented in Figure 28. There is a decrease of the total light of about 3% with a chromatic effect of about 2.5% difference between 350 nm and 1100 nm, quantified by the linear fit in Figure 28. This constitutes the dominant systematics in the CBP throughput measurement.

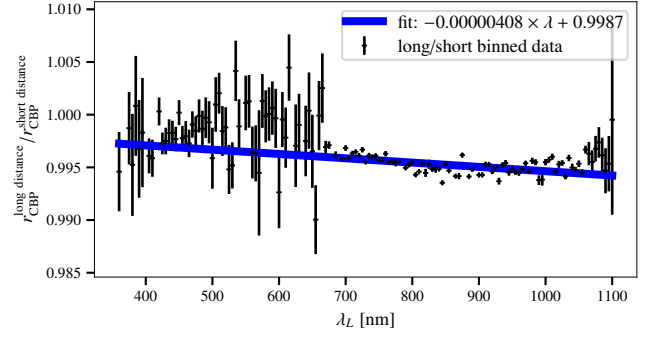


Fig. 28: Ratios of the CBP charge ratio for two different distances to the solar cell as a function of λ_L coming from the 2022/03/08 solar cell run. The long distance is 16 cm larger than the short distance. Black points are the binned ratio for each λ_L , and the blue line is a fit whose equation is in legend.

3.6.7. Repeatability

Finally, we measured the value of the CBP response three times during our measurement campaign. For run i , we computed the CBP charge ratio $r_{\text{CBP}}^{\text{run } i}$, applying dark subtraction and laser contamination correction, binned in 1 nm intervals in λ_L . Then, we computed the mean CBP response $\overline{r_{\text{CBP}}}$ as the mean of the three different runs. We observed ≈ 1 permil differences between the three CBP charge ratios and $\overline{r_{\text{CBP}}}$ (Figure 29), depending slightly with wavelength.

To assess the value of systematic uncertainties on the CBP response due to its stability, we take the maximum absolute distance of the binned ratio to unity in four different ranges of wavelengths (segments the farther from 1 in the bottom plot of Figure 29). The strongest systematics comes from the scattered light.

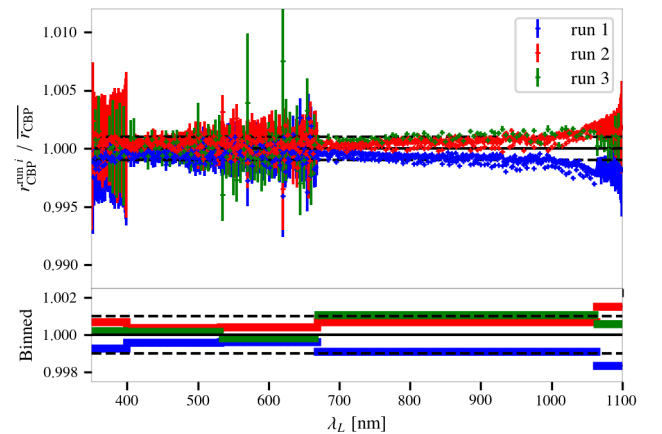


Fig. 29: Ratios of the CBP charge ratio $r_{\text{CBP}}^{\text{run } i} / \overline{r_{\text{CBP}}}$ for three different runs as a function of λ_L . Black dashed lines encompass the per-mil precision region. Top: ratios for each λ_L . Bottom: binned ratio for four different wavelength ranges.

3.6.8. Summary

In summary, we defined the calibrated amount of charges in the solar cell as:

$$Q_{\text{solar}}^{\text{cal}} \equiv Q_{\text{solar}}^{\text{mes}} - Q_{\text{solar}}^{\text{dark}} - Q_{\text{solar}}^{532} - Q_{\text{solar}}^{\lambda_{\text{comp}}} - Q_{\text{solar}}^{\text{fluo}} \quad (31)$$

and in the photodiode as:

$$Q_{\text{phot}}^{\text{cal}}(\lambda_L) = \begin{cases} Q_{\text{phot}}^{\text{mes}}(\lambda_L) - Q_{\text{phot}}^{\text{fluo}}(\lambda_L) & \text{if } \lambda_L < 400 \text{ nm} \\ Q_{\text{phot}}^{\text{mes}}(\lambda_L)(1 + \alpha(\lambda_L)) & \text{if } \lambda_L \in [532, 644] \text{ nm} \\ Q_{\text{phot}}^{\text{mes}}(\lambda_L)(1 + \beta(\lambda_L)) & \text{if } \lambda_L > 1064 \text{ nm} \\ Q_{\text{phot}}^{\text{mes}}(\lambda_L) & \text{elsewhere} \end{cases} \quad (32)$$

All uncertainties from the evaluation of all these terms were propagated. The summary of the error budget on the CBP response is decomposed in Figure 30 as a function of laser wavelength λ_L . Systematics coming from the wavelength calibration are not represented. Indeed, as the CBP response varies slowly with wavelength, it is negligible compared to others. In the visible range, scattered light systematics dominates. In the near-infrared, the subtraction of the λ_{comp} photons is the main systematic uncertainty, while in the UV range, fluorescence correction systematic dominates.

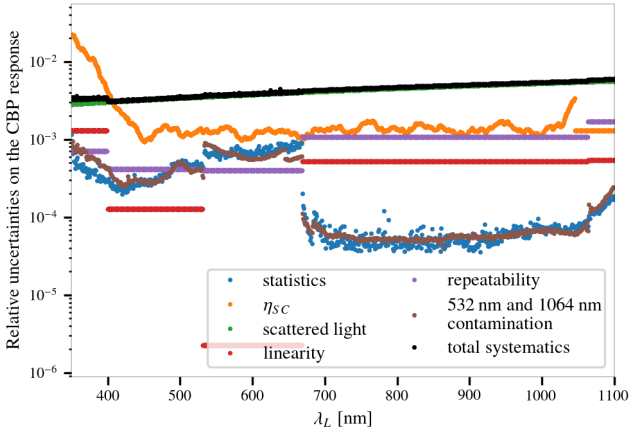


Fig. 30: Total error budget for CBP response. Total systematic budget (black dots) results from the quadratic sum of all the CBP systematic uncertainties (the statistical uncertainties and the solar cell QE uncertainties are excluded here).

3.7. CBP response

The final CBP response in output photons per Coulomb unit in the photodiode is

$$R_{\text{CBP}}(\lambda_c) = \frac{Q_{\text{solar}}^{\text{cal}}(\lambda_c)}{Q_{\text{phot}}^{\text{cal}}(\lambda_c) \times \epsilon_{\text{solar}}(\lambda_c) \times e}. \quad (33)$$

It can be computed for each laser burst. We averaged the values to increase the signal-to-noise ratio and get the red smooth curve presented in Figure 31:

$$\overline{R_{\text{CBP}}(\hat{\lambda}_c)} = \left\langle \frac{Q_{\text{solar}}^{\text{cal}}(\lambda_c)}{Q_{\text{phot}}^{\text{cal}}(\lambda_c) \times \epsilon_{\text{solar}}(\lambda_c) \times e} \right\rangle_{\lambda_c \in [\lambda, \lambda + \delta\lambda]} \quad (34)$$

The average is performed on every burst of the three runs, with a 5σ clipping, and $\hat{\lambda}_c$ the mean calibrated wavelength in a $\delta\lambda = 1$ nm bin. All uncertainties are combined in quadrature (Figure 31 bottom).

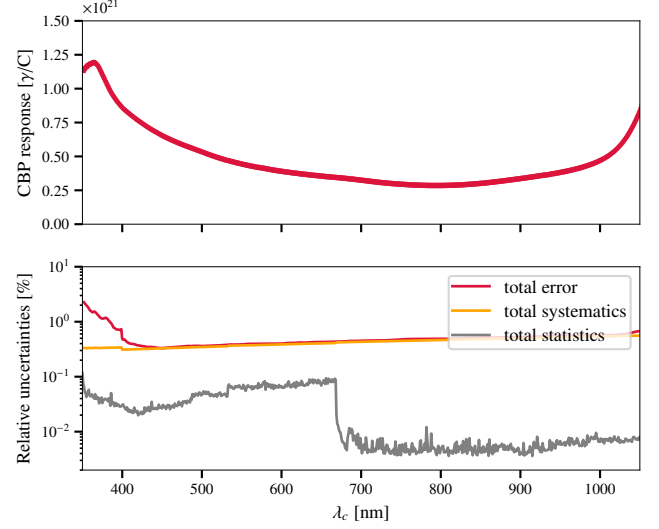


Fig. 31: Top: CBP response $\overline{R_{\text{CBP}}(\hat{\lambda}_c)}$ obtained with the 5 mm pinhole and $\delta\lambda = 1$ nm. Bottom: relative uncertainties.

4. Measurement of the StarDICE telescope response

This section presents the measurement of the StarDICE telescope response $R_{\text{tel}}(\lambda)$ from CBP shoots using the $75 \mu\text{m}$ pinhole. One difficulty is the inter-calibration between the $75 \mu\text{m}$ pinhole and the 5 mm pinhole with which the CBP transmission has been determined in the previous section. Both produce images that are contained in the StarDICE sensor as shown in Figure 32, but the latter form an image of about 250 pixels in radius while the former form an image of about 4 pixels in radius. Their photometry is thus very differently affected by issues such as ghost reflection and light scattered in the tails of the PSF. In this section, we start by building a model of the PSF of StarDICE + CBP, including light's reflection in the optics. We use this model to correct the inter-calibration ratio between the two pinhole sizes, measured with run No. 8 data. We then describe the generic photometry method applied to all other runs using the $75 \mu\text{m}$ pinhole data and present the resulting response measurements.

4.1. Modelisation of the StarDICE PSF on $75 \mu\text{m}$ pinhole data

Figure 33 shows stacks of images obtained with the $75 \mu\text{m}$ pinhole without any filter. The illumination of a section of the primary StarDICE mirror results in a superimposition of the StarDICE telescope PSF and a set of additional fainter images that we call ghosts. The ghosts result from undesired but unavoidable reflections on optical surfaces. The most visible ones come from the beam reflection on the CCD surface and back reflection on its covering window, as described in Figure 34.

For each image in this dataset, we subtract a bias pattern, estimated on a column and row basis, by computing the mean of

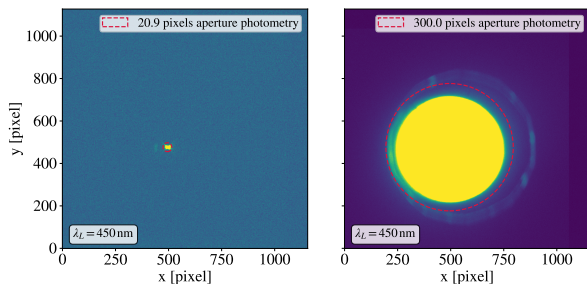


Fig. 32: Examples of images obtained when the CBP shoots in the StarDICE telescope at $\lambda_L = 450$ nm with the 5 mm pinhole on the right and 75 μ m pinhole on the left. The ghost reflection is visible for both images at the left of the main spot. In the 5 mm pinhole image, a large annulus around the main spot is visible and corresponds to light diffusion around the mechanical iris at the input of the CBP.

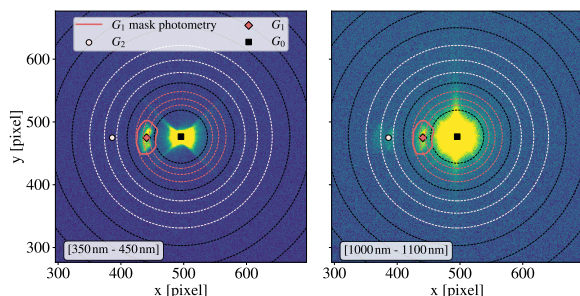


Fig. 33: Stack of images at different wavelengths, with one image per nanometer. *Left*: Stack of images between 350 nm and 450 nm. The scale is set on the ZScale from IRAF to make faint features visible. The spot of interest G_0 is at the center, and the ghost reflections are at its left. The circles correspond to the aperture photometry at different radii. When an annulus contains a ghost contribution, it is colored according to the ghost's order. The red area around the 1st order ghost represents the area where the photometry of the ghost is measured. *Right*: Same image but for a stack of images between 1000 nm and 1100 nm. We note that the 2nd order ghost is not visible for the stack in the UV, where the 1st order is maximal, while it is visible in the IR, where the 1st order is lower.

the horizontal and vertical overscans. We compute the centroid of the signal and then perform aperture photometry by summing pixels within a radius $r = 20.9$ pixels, and then for successive annulus of external radius from 24.9 pixels to 419.1 pixels. These radii are regularly spaced on a logarithm scale shown in Figure 33.

We model the StarDICE telescope PSF as the sum of a Moffat function, a constant background level, and contributions from ghosts at specific distances from the main spot. The Moffat function (Moffat 1969), integrated in an aperture of radius r , reads:

$$M(r, \lambda) = 1 - \left(1 + \frac{r^2}{\alpha(\lambda)^2}\right)^{-\beta(\lambda)}, \quad (35)$$

with $\alpha(\lambda)$ and $\beta(\lambda)$ the scale and exponent parameters of the Moffat distribution, which depend on the wavelength. The flux

$F(r, \lambda)$ measured in the CCD with aperture photometry can then be modeled as:

$$F(r, \lambda) = A(\lambda) \times \frac{M(r, \lambda) + K_{G/A}(r, \lambda)}{1 + K_{G/A}(r \rightarrow +\infty, \lambda)} + \pi r^2 bkg(\lambda), \quad (36)$$

with $A(\lambda)$ the total amplitude, $K_{G/A}(r, \lambda) = \frac{\sum_{n=1}^{+\infty} G_n(\lambda)}{A(\lambda)}$ the relative contribution of the sum of all the ghosts $G_n(\lambda)$, and $bkg(\lambda)$ the background level in ADU/pixel.

The evolution of the Moffat distribution is smooth with respect to wavelength. We therefore develop the parameters $\alpha(\lambda)$ and $\beta(\lambda)$ on a B-spline basis with 15 wavelength nodes regularly spaced between 350 nm and 1100 nm. The same applies to the function $K_{G/A}(r, \lambda)$ as it corresponds to light reflections on surfaces in the optical path. This reduces the number of free parameters and allows us to perform outlier rejection of a few annulus whose photometry was affected by a cosmic ray (9 photometric points affected out of 13122 measurements). The fit results are shown in Figure 35.

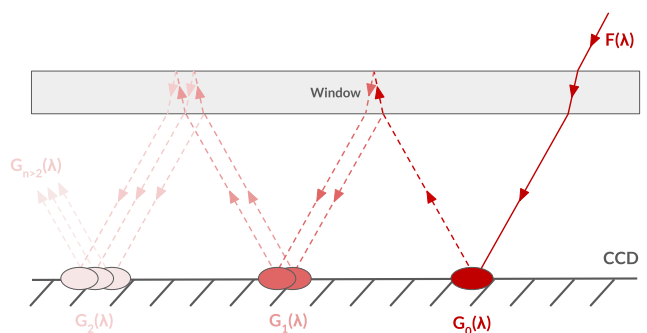


Fig. 34: Schematic of the light reflections that generate the ghosts, which are defocused and less intense images at other positions in the focal plane. A fraction of the light is reflected at the different interfaces, and $G_0(\lambda)$, $G_1(\lambda)$ and $G_2(\lambda)$ are respectively the main spot, the 1st order ghost, and the 2nd order ghost.

The most striking result is a significant degradation of the PSF after 950 nm, apparent in the steep decrease of the value of the β Moffat parameter and the increase of the α parameter presented in the first and second panels. This effect is also visible when comparing the two stacks in Fig. 33. We were not able to pin down the exact origin of this degradation. A potential explanation could be that one of the reflective surfaces becomes partially transparent at these wavelengths and generates diffused light. The consequence of this effect on photometry will be further discussed in Section 4.4.

The $\alpha(\lambda)$ and $\beta(\lambda)$ best-fit parameters are otherwise fairly stable between 350 nm and 900 nm. The third panel shows the background level reconstructed across all wavelengths. With a mean of $\mu_{bkg, fitted} = 0.267$ ADU/pixel for an exposure time of 1.1 s, it is very consistent with the values measured on dark images. Two datasets of dark images have been studied, one with the laser turned off and a second by masking the CBP output with a cap (dataset No. 9 in Table 2). Both datasets show no trend in time or wavelength and have a mean value of $\mu_{dark, photometry} = 0.252$ ADU/pixel and a standard deviation $\sigma_{dark, photometry} = 0.059$ ADU/pixel, represented by the black dashed line and shaded area in this third panel.

The fourth panel presents the relative contribution of the first order ghost $G_1(\lambda)$, $K_{G_1/A}(\lambda) = \frac{G_1(\lambda)}{A(\lambda)}$ in percent. We compared these reconstructed values with direct photometry of the

visible first-order ghost pattern performed in 2D images as detailed in Appendix A. This more direct determination of the ratio $K_{G_1/G_0}(\lambda)$ is shown as the dashed black line. The two different methods match perfectly up to 950 nm showing that the identified ghost constitutes the only significant deviation from the Moffat profile. Beyond 950 nm, the second method does not give accurate photometry for the ghost because it starts to be mixed with the core of the PSF.

The fit reduced chi-squared of 1.86 is explained by the fact that the Moffat shape does not describe the complex shape of the PSF core. To mitigate this issue, and as we are mainly interested in modeling the tails of the PSF, we start our profile modeling at a rather large inner aperture of 20.9 pixels, where residuals no longer display visible structure, and the chi-square displays no trend in wavelength. Going to a larger inner aperture increases the quality of the fit but decrease its stability as the scale parameter α is no longer properly constrained.

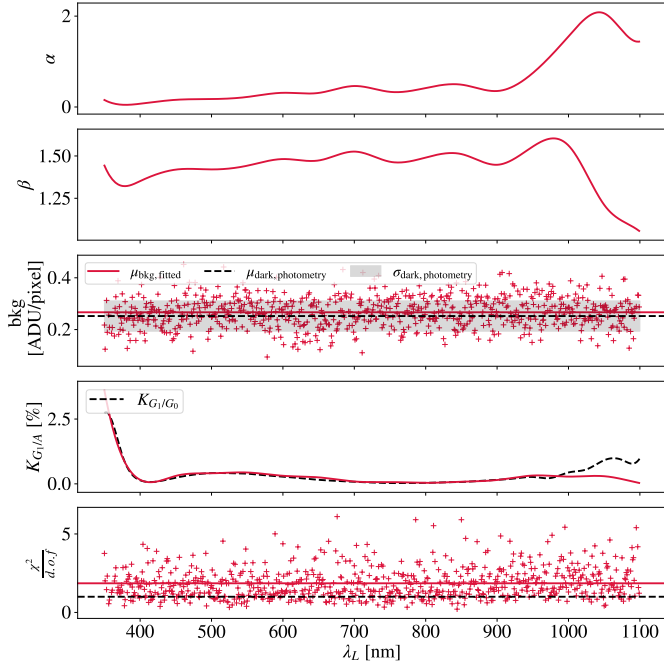


Fig. 35: Best fitting parameters for the model of Equation 36. Red plain lines correspond to the result of the fit, and black dashed lines, when applicable, correspond to the values expected. From top to bottom: the first and second panels represent respectively the $\alpha(\lambda)$ and $\beta(\lambda)$ parameters from the Moffat distribution; the third panel shows the background contribution per pixel and its mean value in red, while the dark dashed line is the mean value of the dark; the fourth panel represents $K_{G_1/A}(\lambda)$, and $K_{G_1/G_0}(\lambda)$; the fifth panel represents the reduced chi-squared of the fit.

4.2. Accounting for CBP light contamination

As for the photodiode and the solar cell (see Sections 3.6.3 and 3.6.4), the total signal measured in the StarDICE camera $Q_{\text{ccd}}^{\text{mes}}$ is the sum of the flux from the main laser line $Q_{\text{ccd}}^{\text{cal}}$ and the flux from the 532 nm contamination Q_{ccd}^{532} , the λ_{comp} contamination $Q_{\text{ccd}}^{\lambda_{\text{comp}}}$, and the integrating sphere fluorescence $Q_{\text{ccd}}^{\text{fluo}}$, as follows:

$$Q_{\text{ccd}}^{\text{mes}} = Q_{\text{ccd}}^{\text{cal}} + Q_{\text{ccd}}^{532} + Q_{\text{ccd}}^{\lambda_{\text{comp}}} + Q_{\text{ccd}}^{\text{fluo}} \quad (37)$$

The contamination light in the StarDICE camera can be estimated by multiplying Q_{phot}^{532} , $Q_{\text{phot}}^{\lambda_{\text{comp}}}$ and $Q_{\text{phot}}^{\text{fluo}}$ measured with the CBP photodiode by a first estimation of $R_{\text{CBP}}(\lambda)$ and $R_{\text{tel}}(\lambda)$. We then refine the measurement of $R_{\text{tel}}(\lambda)$ and correct iteratively the effect of those contaminations.

The effects of this procedure are most clearly demonstrated by its impact on the StarDICE g filter transmission measurement, as presented in Figure 36. This measurement is particularly susceptible to contamination from integrating sphere fluorescence and the 532 nm line. Our results indicate that contamination is responsible for the apparent out-of-band transmission of the filter, which completely disappears once contributions at contaminating wavelengths are corrected.

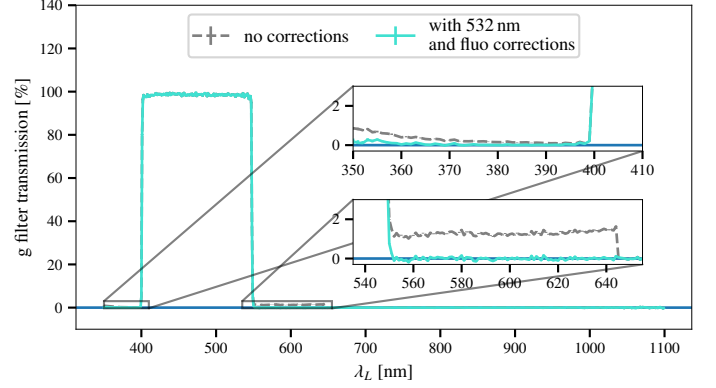


Fig. 36: StarDICE g filter transmission as a function of the set laser wavelength λ_L , with and without the 532 nm and fluorescence correction. For clarity, we added zooms on the out-of-band transmissions where contamination light is transmitted while the main wavelength is blocked.

4.3. Pinhole intercalibration

Given that we utilize different pinholes for measuring the CBP and StarDICE responses, it is necessary to intercalibrate the CBP response with both pinholes. The CBP response R_{CBP} , as defined in Equation 2, can be expressed as follows:

$$R_{\text{CBP}}(\lambda) \equiv R_{\text{CBP}}^{75\mu\text{m}}(\lambda) = R_{\text{CBP}}^{5\text{mm}}(\lambda) \times K_{75\mu\text{m}/5\text{mm}}(\lambda), \quad (38)$$

with $K_{75\mu\text{m}/5\text{mm}}(\lambda)$ the inter-calibration term and $R_{\text{CBP}}^{75\mu\text{m}}$ (resp. $R_{\text{CBP}}^{5\text{mm}}$) the CBP response measured with the 75 μm pinhole (resp. 5 mm pinhole).

We estimate the correction term $K_{75\mu\text{m}/5\text{mm}}(\lambda)$ as the ratio of the StarDICE responses obtained with both pinholes in runs No. 8. The 5 mm pinhole photometry is performed as follows. The background is estimated with dark exposures from the dark datasets, and the spatial mean of all these dark images is computed to obtain a master dark. When performing aperture photometry on the 5 mm image, we subtract a background equivalent to the aperture photometry of the master dark at a similar position and radius, obtaining $Q_{\text{ccd}}^{5\text{mm}}$. The optimal radius is evaluated at 300 pixels for the 5 mm pinhole to contain the main spot and the 1st order ghost. Figure 37 shows the StarDICE response obtained with the 5 mm pinhole and no filter.

We estimate the pinhole flux, $F(300, \lambda)$, as the flux obtained by integrating the best-fit model (Equation 36) within a 300-pixel aperture. This approach ensures that we compare the StarDICE responses for both pinholes at an equivalent radius,

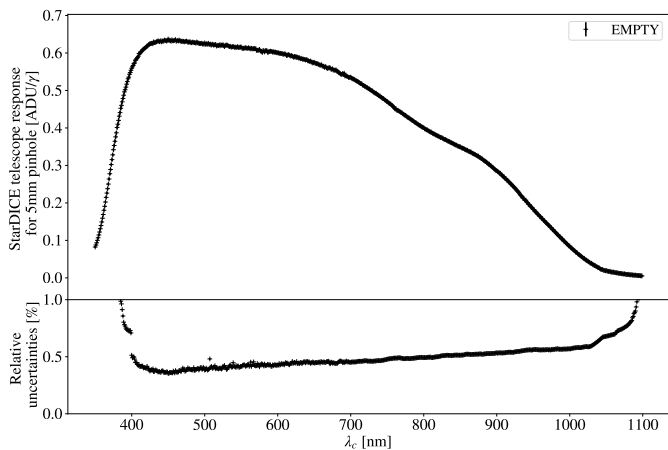


Fig. 37: *Top*: StarDICE response with no filter and 5 mm pinhole with respect to wavelength in nanometer. *Bottom*: Uncertainties over the StarDICE response measurement with respect to wavelength in nanometer.

thereby incorporating identical features of the point spread function (PSF) while maintaining a favorable signal-to-noise ratio for the fainter pinhole. The ratio $K_{75\mu\text{m}/5\text{mm}}(\lambda) = \frac{F(300)}{Q_{\text{ccd}}^{5\text{mm}}}$ is presented in Figure 38.

The noticeable oscillations in wavelength observed in this ratio starting at 900 nm are attributable to fringes present in the CCD, which significantly impact the 75 μm pinhole measurement but have a lesser effect on the large pinhole as most average out over the large surface of the pinhole image. Apart from this phenomenon, which is unrelated to a change in the CBP transmission, a slight chromatic change in the measured ratio cannot be attributed to differences in photometry. We attribute this change to an effective modification in $R_{\text{CBP}}(\lambda)$ upon switching pinholes and model it as a linear function of wavelength. We fit this function in the range 400 nm to 900 nm where the ratio measurement is clean. This function is utilized for recalibrating the CBP transmission with the 75 μm pinhole, as described in Equation (38), throughout the remainder of this analysis.

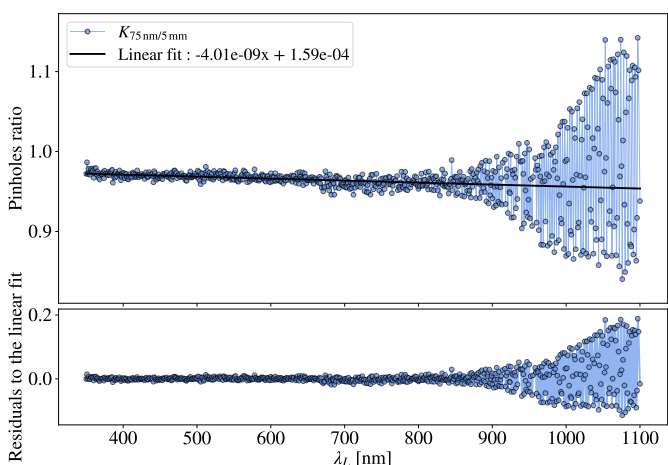


Fig. 38: Ratio $K_{75\mu\text{m}/5\text{mm}}(\lambda)$ as a function of wavelength, relative to the prediction given by the ratio of the nominal area of the pinholes. The black line corresponds to a linear fit between 400 nm and 900 nm.

4.4. Photometry applicable to on-sky data

The measurement of the PSF at a long distance from its core is possible in CBP images because of the shallow level of background light in these images. It is impractical to port this method to on-sky data. We choose to carry out the throughput measurement for an aperture photometry and a background estimation algorithm applicable to on-sky data.

The photometry is performed as follows. To estimate the background contribution, the sources in the image need to be detected and masked. We compute the standard deviation of an image σ , and every pixel with a signal higher than 5σ is masked, as well as all the surrounding pixels with a signal higher than 2σ . Then we proceed to a segmentation of the masked image into boxes of 129×132 pixels (corresponding to $\sim 3.6 \text{ arcmin} \times 3.6 \text{ arcmin}$). We compute the mean and the standard deviation of the background in each of these boxes, and we interpolate their values in a 2D map to get our estimation of the background. This background estimation is subtracted from the image. Then, the centroid of the spot of interest is computed as the Gaussian-weighted first moment of the flux to pursue aperture photometry at this position. Q_{ccd} is measured with aperture photometry at a radius of 20.9 pixels for every image of the dataset with the 75 μm pinhole.

Based on the model built in Sect. 4.1, we can quantify the fraction of the total flux measured in 75 μm pinhole images with this aperture photometry method. We define the fraction of flux missed as the ratio between the value measured with aperture photometry for a given radius and wavelength and the total amplitude A fitted with the method detailed in the previous section for the same wavelength. The result is the blue curve in Figure 39. About 98% of the flux is collected between 400 nm and 900 nm. The ghost contribution, which is missed when using an aperture of 20.9 pixels, contributes about another extra percent to the missed flux below 400 nm. Above 900 nm where the PSF is degrading fast, the fraction of flux missed increases by one order of magnitude and reaches more than 75% at 1050 nm.

While most of this effect is directly explained by the aperture correction, a small contribution also comes from a bias in the background estimate caused by the pollution of the background map by the source PSF tails. Given that the model of the PSF predicts the value of the aperture correction (red curve in Fig. 39), we can estimate the contribution of the background bias as the difference between the two curves. This curve, presented in the bottom panel of Fig. 39, shows that the background bias contributes about 0.2% of the total flux.

We conclude that the instrument response determined for our large aperture photometry of the 75 μm pinhole is likely to apply to similar star photometry with minimal aperture corrections in the range between 400 nm and 900 nm. Below 400 nm, there will be a need to consider the ghosting pattern for the full aperture, which will mix partially with the photometry aperture. Above 900 nm, our method is unlikely to give a representative determination of the instrument's response to star flux. At this stage, we think that the StarDICE telescope is responsible for the PSF degradation, with one possible explanation being that the primary mirror becomes partially transparent and generates diffused light. Further discussion of the applicability of the measured transmission to on-sky data will require a study of the PSF on stellar images, which is left for future work.

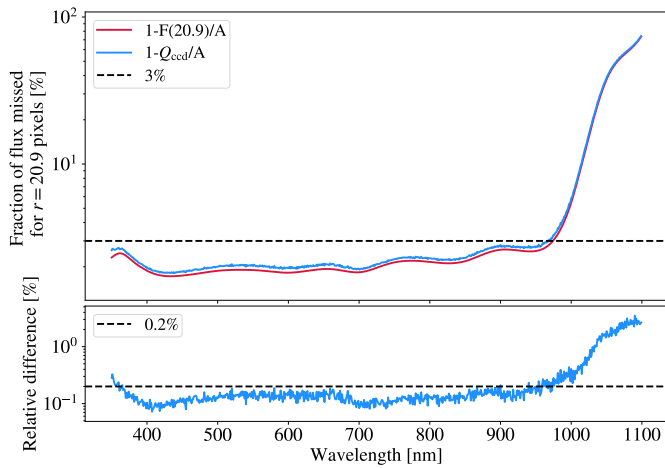


Fig. 39: *Top*: Fraction of missing flux against λ_L when measuring $75\ \mu\text{m}$ pinhole dataset with aperture photometry at 20.9 pixels rather than taking the total amplitude A fitted. The red curve corresponds to the estimation of the fit and the blue one to aperture photometry when the background is estimated with the method described in Section 4.4. *Bottom*: Relative difference in percent between the flux measured for aperture photometry with the two background estimations and the model estimation at 20.9 pixels.

4.5. Results

4.5.1. StarDICE response and filter transmissions

We measured the StarDICE response with the empty slot of the filter wheel, the transmission of the *ugrizy* filters, and the grating transmission with dataset No. 6, using the $75\ \mu\text{m}$ pinhole, shooting at a fixed mirror and focal plane position. Figure 40 shows the results obtained, following the procedure based on aperture photometry. We note that the wavelength coverage does not scan the entire passband of the *u* filter. Filling the gap between our measurements and the atmospheric UV cut-off would need additional measurements that are out of the scope of this paper.

After accounting for the relative uncertainties, we demonstrate a precision of $\sim 0.5\%$ per bin of 1 nm for all the filter transmissions, the empty filter wheel slot, and the 1st order of the diffraction grating from 400 nm to 950 nm. The 0.2 nm wavelength accuracy of our measurements is illustrated by the fine resolution of the sharp filter edges.

4.5.2. StarDICE Responses variations

Since the CBP only illuminates a portion of the primary mirror, we need several measurements at different positions to span the full transmission of the StarDICE telescope. Dataset No. 2, where we point at 4 different positions along the primary mirror radius, and No. 3, where we point at every one of the four quadrants of the primary mirror, have been acquired specifically to investigate these variations. We also explored the small-scale variations over the focal plane with dataset No. 12, where we made slight pointing changes around a fixed position.

Figure 41 is divided into two panels. The left panel exhibits the results of transmission measurements taken at various radii (corresponding to dataset No. 2). In contrast, the right panel displays the spatial variations in these measurements across the focal plane (representing dataset No. 12).

We display the average behavior for both datasets by fitting a smooth spline through the different measurements. The varia-

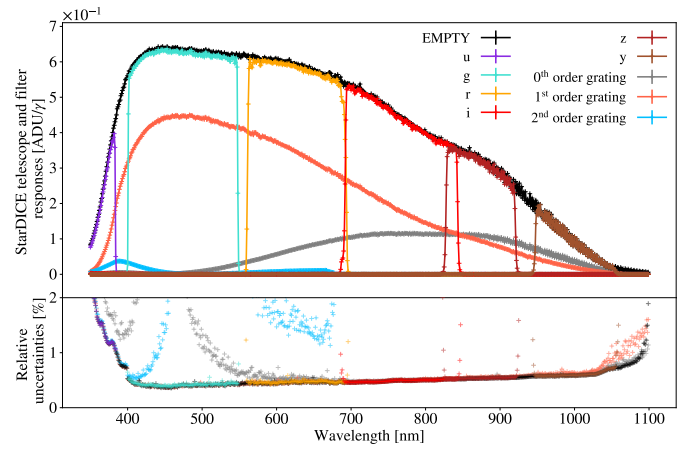


Fig. 40: *Top*: StarDICE response against wavelength in nanometer, with the empty filterwheel slot; all *ugrizy* filters; and the 0th, 1st and 2nd order diffraction of the grating. All of these responses have been measured with the $75\ \mu\text{m}$ pinhole. *Bottom*: Relative uncertainties over the StarDICE response measurements against wavelength in nanometer.

tions above 900 nm are due to small-scale variations caused by interference fringing in the detector. As expected, the impact is larger when the optical path differences between measurements are smaller, i.e., when we explore the variations over the focal plane (right panel). We also note the yellow curve being off the mean spline by $\sim 1\%$, corresponding to a local non-uniformity in the focal plane, but we haven't investigated this aspect yet.

The most striking feature of Figure 41 needing discussion is the significant (20%) variation of transmission measured in the different quadrants of the primary mirror below 400 nm. We didn't reach a firm conclusion concerning the explanation of this behavior. Still, the more solid assumption is that it might be explained by the Hilux coating⁶ on the StarDICE mirrors, whose reflectivity varies with the light incidence angle. This significant effect prevented us from making good use of the measurement in the 4 telescope quadrants (dataset No. 3) as the radius corresponding to those measurements could not be determined with sufficient precision, which impact will be quantified in Section 5.3.

In the 400-900 nm region, the variations over the focal plane and between primary mirror positions are below the percent level. This relative homogeneity of the telescope response allows us to pursue the modeling of the full pupil response of the instrument expecting a reasonable accuracy without the need of additional data, as discussed further in section 5.

Also, regarding the modeling of the full pupil transmission, figure 42 shows the measurement of the expected interference filter edges shift caused by the incident light angle variation when we illuminate the primary mirror at different radii. The figure shows the edges of the *g* and *r* filter in the top panel, and of the *z* and *y* filters in the bottom panel as measured when illuminating four different radial positions in dataset No 2. The edges are noticeably bluer at higher radial positions, which correspond to higher incidence angles, illustrating how the accuracy of those measurements allow us to consider their interpolation to obtain the full pupil transmission of the telescope.

⁶ <https://www.orionoptics.co.uk/optical-coatings/>

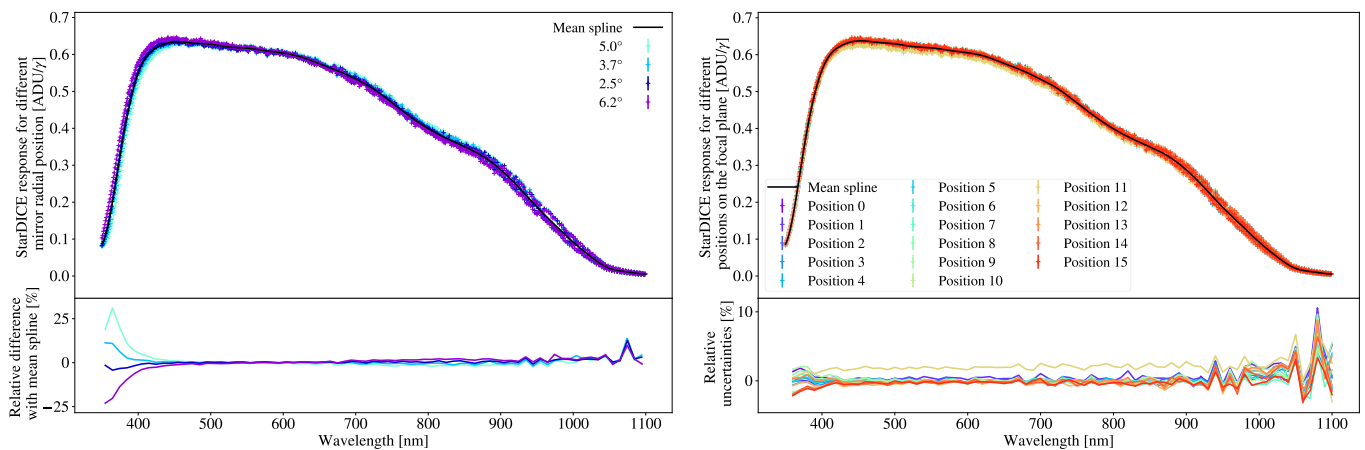


Fig. 41: *Top*: StarDICE response for the different radial positions on the mirror with a fixed focal plane position (left) and different focal plane positions with a fixed mirror position (right). The colors in the left plot match with positions illustrated in Figure 7, while each color in the right plot represents a position on the focal plane. In both plots, the black dashed line corresponds to the mean spline. *Bottom*: Relative difference between the data and the mean spline, binned to a 10 nm resolution to smooth the effect of fringing.

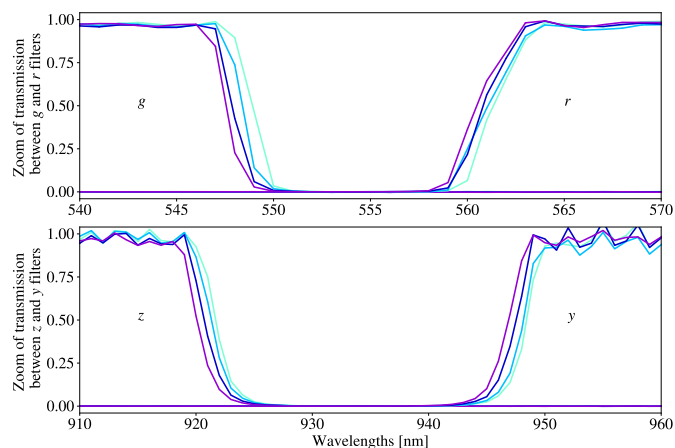


Fig. 42: Zoom on the StarDICE filter transmissions measured at different radial positions on the mirror, between the g and r filters (top panel) and the z and y filters (bottom panel). The colors correspond with the radius labeled in Figure 7.

5. Synthesis of the equivalent transmission for full pupil illumination

The telescope's reflectivity and the filters' transmission exhibit a distinct radial dependency. Although the filter transmission dependence is expected due to its interferometric nature, the origin of the telescope reflectivity dependence remains unclear. Despite this, we can construct an empirical model that assumes smooth transitions between measurements and calculate the theoretical "full pupil" transmission by averaging the model over the illuminated portion of the primary mirror. These two steps are necessary to achieve sub-percent color accuracy and sub-nanometer precision in central wavelengths determination.

We also estimate statistical and systematic errors in the final transmission curves and propagate them through the analysis process. A better understanding of these errors in interpreting broadband photometry is obtained using the spectrophotometric standard star G191B2B as a sample star.

5.1. Radial model of the instrument transmission

The open transmission of the telescope is modeled as a smooth 2D function of wavelength and incidence angle. The function is defined on a basis of cubic B-splines, with 35 regularly spaced wavelength nodes covering the range from 350 nm to 1100 nm, and two nodes at angles corresponding to the inner and outer edges of the occultation-free primary mirror, ranging from 1.97° to 7.24° . These angles represent radii of 55 mm to 203 mm for a primary mirror with a focal length of 1600 mm.

For data acquired using a filter, we multiply the open transmission model by a model of the interference filter transmission, defined as follows:

$$T(\lambda, \theta) = \mathcal{T} \left(\frac{\lambda}{\sqrt{1 - (\sin(\theta)/n_{\text{eff}})^2}} \right). \quad (39)$$

Here, n_{eff} is an effective index for the filter, and \mathcal{T} is a piece-wise linear function of wavelength. The piece-wise linear function is initially created with 150 regularly spaced nodes between 350 nm to 1100 nm, providing a general resolution of 5 nm. In cases where more precision is needed, we further refine the grid by equally splitting intervals where the local mean chi-square exceeds the global mean chi-square by more than three standard deviations. This process is repeated four times to ensure that filter fronts are typically modeled with up to approximately 0.3 nm resolution.

In the specific case of the grating zeroth and first orders, the photometry is adjusted using a cubic B-spline model with 105 nodes in wavelength.

The composite model is fit to dataset No. 2, which includes data from four different radii and successive observations without filters or with all seven filters and the grating. The baseline model has 1979 free parameters: 148 for the open transmission, approximately 6×165 for each of the $ugrizy$ filters, and 420 for each of the grating orders. Unfortunately, the blue edge of the u -band filter cannot be accurately measured with this data. Fit results are displayed in Fig. 43.

Overall, the model provides a satisfactory description of the dataset. The most significant discrepancy is a noticeable gray decrease in the transmission of the r filter for the sample measurement at 3.7° with respect to the average of the other three. Af-

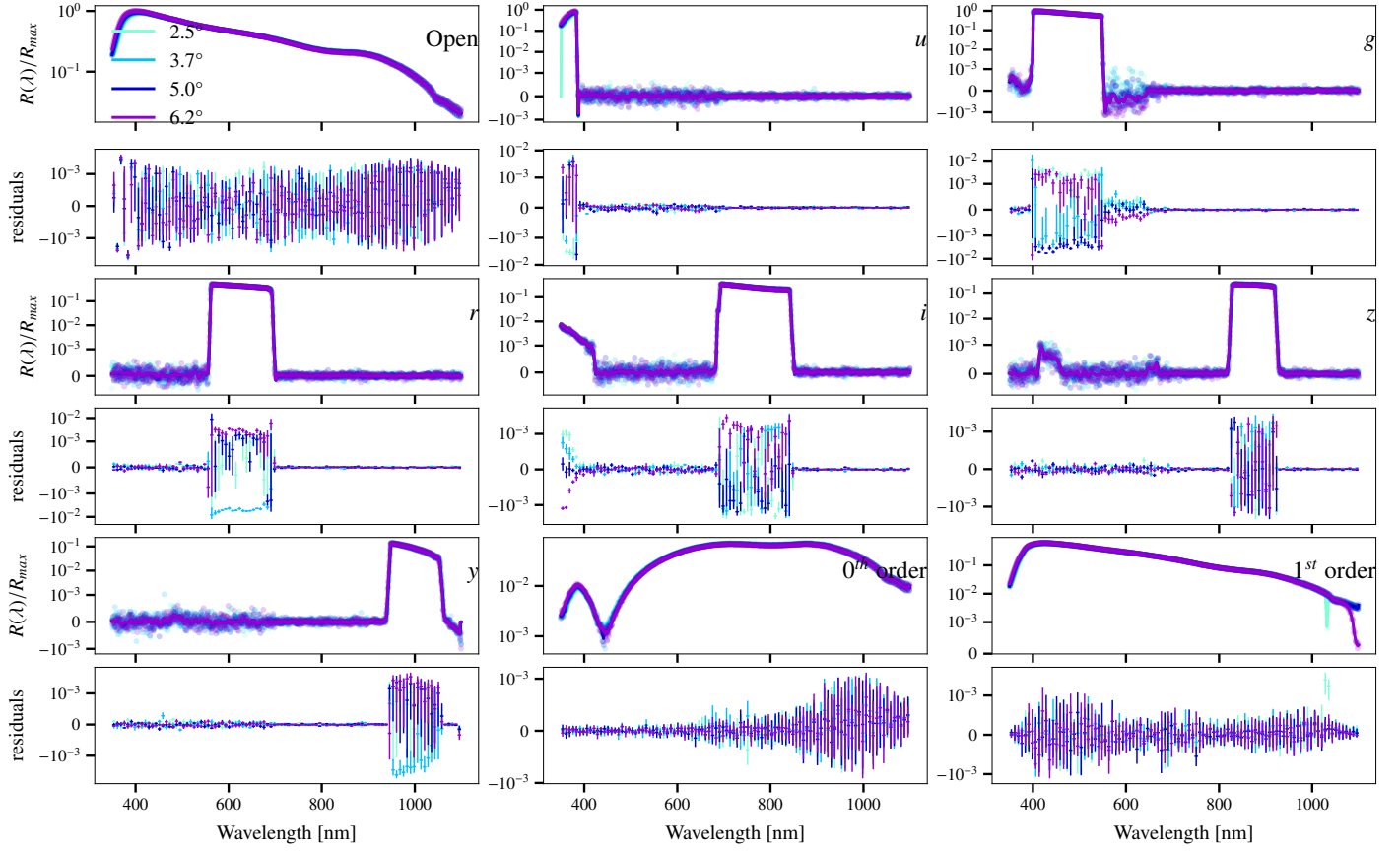


Fig. 43: Model of the wavelength and radial dependency of the StarDICE response to CBP illumination $R(\lambda)$. Each panel display the raw measurements at the 4 sampled positions for each of the filter configurations: no filters (Open), with one of the 6 photometric filters (*ugrizy*) or with the grating looking either at the zeroth order or the first order spots. The panel immediately below each panel display the residuals to the model as a fraction of the data. For easy comparison, all panels are normalized to the peak of the response, which occurs in the open configuration at $\lambda = 398$ nm and $\theta = 6.2^\circ$.

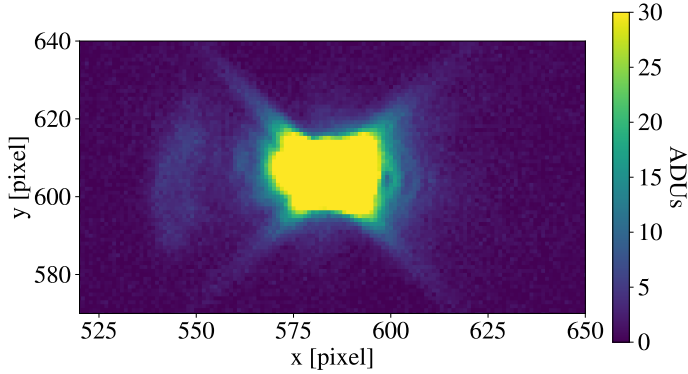


Fig. 44: Diffraction rings due to the presence of a dust spot on the *r* filter, intercepting the CBP beam.

ter investigating this issue, we identified that the corresponding images displayed a diffraction figure consistent with the presence of a dust particle on the filter surface intercepting the CBP beam, visible in Figure 44. Based on the approximate area of the beam spot (~ 12 mm²), and the estimated particle size range (between 200 μ m to 300 μ m), we calculated a potential decrease in transmission for this specific partial illumination of the primary mirror of up to 0.6%. This value is in good agreement with the observed decrease. Similar discrepancies were found for some observations in *u*, *g*, and *y* bands, although determining particle

sizes from diffraction features was not possible in these cases. We attribute these discrepancies to dust contamination on the filter surface as well.

The top panel of Fig. 45 shows the difference between the transmission integral for measurements and the model at each position, helping readers better visualize the 'gray' discrepancies. The standard deviation of the model/measurement discrepancies is 10.2 mmag. Considering this value as an estimate of dust-induced dispersion, we can deduce that the corresponding uncertainty for per-filter normalization of the model (averaging 4 independent samples) is approximately 5 mmag.

This noise could be decreased by averaging more sample measurements of the mirror. In our case 4 additional positions were sampled as part of run 3 (see table 2). However, while measurements of run No. 2 were carefully taken to sample the mirror from the outer edge to the inner edge along a radius with separations provided by the mount encoders, the other measurements were positioned semi-randomly with the idea that the position of the CCD-window ghost in the images will enable precise determination of the position of the beam in the mirror. Two issues were overlooked at this stage which complicated the determination of the geometry from the position of the ghosts: (1) The wedge of the CCD window and (2) the ghost position dependence on the conjugation relation between the CBP and the telescope which is only approximately known. The complexity of including those parameters in a full model of the telescope+CBP

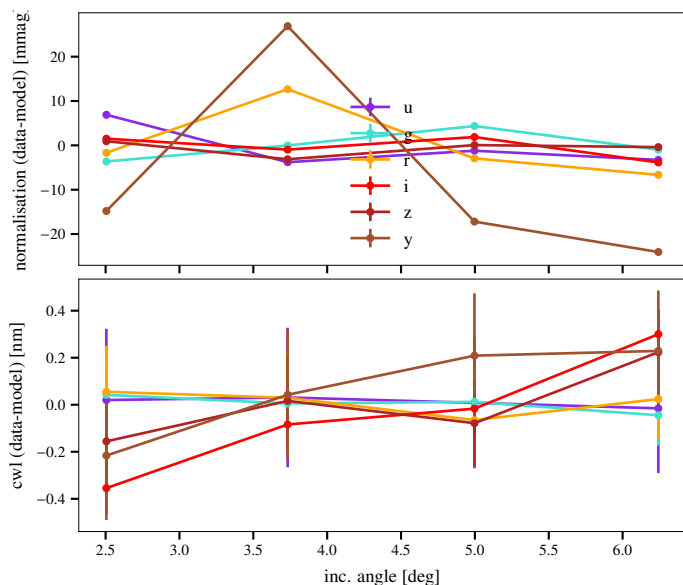


Fig. 45: Discrepancies between model and raw measurements at different mirror locations summarized according to 2 metrics: *Top*: relative difference in the integral of the passband, expressed in millimagnitudes; *Bottom*: relative difference in central wavelength computed as the barycenter of the passband.

sets the analysis of those data out of the scope of the current paper.

The bottom panel in Fig. 45 displays the difference between the measured central wavelength and the model-predicted value for all 4 radius positions. The model accurately reproduces the central wavelengths of all filters with a standard deviation of only 0.13 nm. This represents an improvement by an order of magnitude compared to a model that neglects wavelength shift considerations due to the light incidence angle on the filter, highlighting the importance of including this effect in the StarDICE response model.

5.2. Full pupil synthetic transmission curves

The full pupil transmission is synthesized by numerically averaging the above model assuming that the pupil is a perfect annulus with an inner radius of 55 mm and an outer radius of 203 mm, corresponding to an effective mirror area of 1202 cm². The rectangle rule with 100 evenly sampled points in radius has been used for the averaging. The curves have been normalized using the CBP response from Sect. 2.2. The resulting transmission curves are shown in Fig. 46.

5.3. Final uncertainty budget

The impact of the uncertainties in our determination of the full-pupil transmission curves depend on the application. We first consider the use of the CBP as the sole source for absolute calibration of the instrument response and then its use in conjunction with a broadband star-like calibration light source.

5.3.1. Uncertainties in absolute fluxes

The first obvious application is to take each curve as an absolute calibration of the instrument throughput and use it to interpret broadband fluxes measured by this instrument, according to the

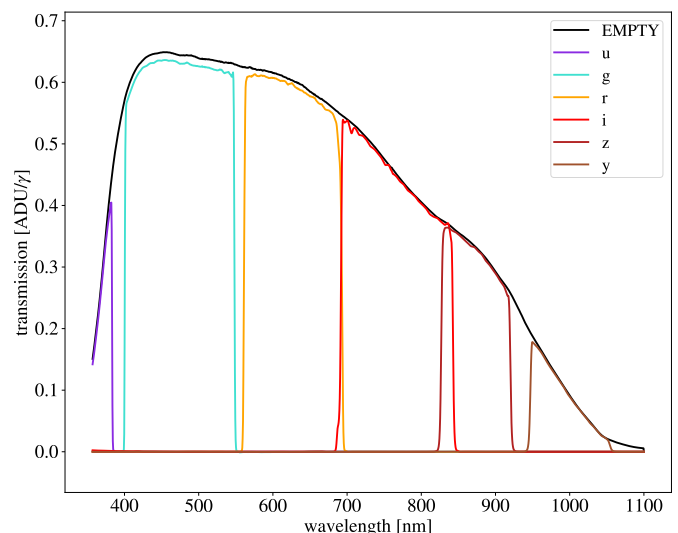


Fig. 46: Full-pupil transmission curves for the StarDICE instruments.

equation:

$$\phi_b = \int_{\lambda} R_b(\lambda) A(\lambda) S(\lambda) d\lambda \quad (40)$$

where R_b is the full pupil response curve of the instrument synthesized previously, S is the top of the atmosphere spectrum of the target and A is the atmospheric transmission for this observation. Setting aside the question of the atmospheric transmission, the error δR_b on the passband will translate into an error on the synthesized flux $\delta\phi$, whose magnitude depends on the spectrum of the object. As an illustration we propagated all our uncertainties to the synthetic fluxes of the primary spectrophotometric standards G191B2B. We report the results in Table 3 as the relative uncertainty on the broadband flux $\sigma(\delta\phi)/\phi$ for each band, with one line per contributions. The table does not include the uncertainty on the gray scale, mainly coming from the uncertainty in the effective area of the telescope which cannot be determined accurately with such a setup.

The dominant contributor to the uncertainty in our flux reconstruction is the mirror sampling noise. With the CBP beam sampling only a small fraction of the primary mirror, and therefore a small fraction of the filters, any inhomogeneity in the transmission of the filter ends up causing a noise in the band-to-band ratio of transmissions. This noise decreases with more sampling points on the primary mirrors, at a large observational cost.

The next significant issue is the difficulty of getting rid of non-collimated (scattered) light during the calibration of the CBP on the solar-cell array. A natural way to deal with this issue would be to significantly increase the solar-cell CBP distance. In our case, however, the beam created by the 5 mm pinhole already barely fit inside the footprint of the solar cell. Increasing the solar-cell CBP distance would have caused issues for the collimated beam calibration in exchange for getting rid of the non-collimated light.

Some caution needs to be paid to changes in the working temperature of photodiodes when calibrating the y band. In our current measurement, the uncertainty in the difference in temperature between the calibration of the solar cell and its use to calibrate the CBP is quite large (1.6 °C). This has easily been

Table 3: Relative uncertainty in the synthetic broadband fluxes of G191B2B, split by contributions, in permil.

Source	u^\dagger [‰]	g [‰]	r [‰]	i [‰]	z [‰]	y [‰]
StarDICE	0.5	0.2	0.2	0.3	1.0	3.8
ϵ_{SC}	1.6	0.1	0.1	0.1	0.1	0.1
CBP	2.2	0.5	1.2	0.0	0.0	0.1
Stat (total)	2.7	0.5	1.2	0.3	1.0	3.8
Scattered light	2.7	3.1	3.8	4.3	4.8	5.3
Repeatability	0.8	0.4	0.5	1.1	1.1	1.1
Linearity	0.2	0.2	0.3	0.5	0.5	0.5
Contamination	4.4	0.6	0.8	0.1	0.1	0.1
Mirror sampling noise	5.4	5.4	5.4	5.4	5.4	5.4
NIST photodiode	0.2	0.1	0.0	0.0	0.0	0.1
Solar cell temperature	0.0	0.0	0.0	0.0	0.0	3.9
Wavelength calibration	0.7	0.6	0.5	0.4	0.3	0.3
Syst (total)	7.6	6.3	6.7	7.1	7.4	8.7
Total	8.0	6.3	6.8	7.1	7.5	9.4

Notes. † Our measurement does not capture the blue side of the u band filter. We propagate uncertainties as if the transmission was dropping to 0 at the edge of the measurement to illustrate the performances that would be obtained from a complete measurement. For all practical purposes, however, the actual u band transmission cannot be determined from the existing measures.

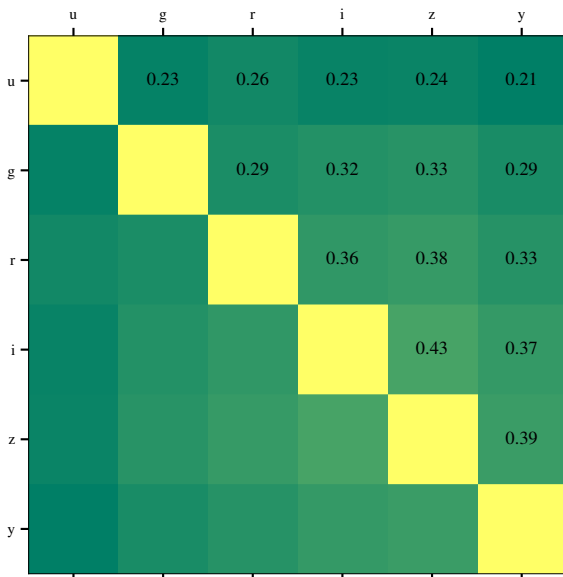


Figure 47: Correlation of the uncertainties on the synthetic fluxes of G191B2B.

fixed in the latter iteration of the solar-cell design by including temperature sensors directly cell enclosure.

Our mitigation procedure for the contamination of the beam by light at different wavelengths is found satisfactory for all bands but u . This is due to the remaining uncertainties in the determination of the phosphorescence contribution in the integrating sphere.

Lastly, most systematic uncertainties have modes coherent across wavelengths. As a result, the errors induced on broadband magnitudes are correlated across bands, with typical correlation

levels in the 20-40% range. The correlation matrix resulting from the full propagation of uncertainties identified in Table 3 is displayed in Fig. 47. Again, we do not account for the uncertainty in the gray scale which is perfectly correlated between all bands and would dominate the uncertainty budget.

5.3.2. Uncertainties in relative fluxes

The more common application of telescope transmission measurements is to rely on the transmission curves to predict actual observations of a spectrophotometric standard of known flux and determine an independent re-calibration factor for each band. The errors on the interpretation of observations of another object will then depend on the difference in color between the object and the spectrophotometric standard, canceling for objects whose spectrum is very similar to the spectrum of the standard.

For the StarDICE telescope, the role of photometric standard is played by a collection of narrow-spectrum LEDs, whose observations set the absolute normalization of each band. The telescope is then used to observe CALSPEC standard stars and precisely measure their broadband fluxes, anchoring them to the LEDs absolute calibration. In this operation, all uncertainties which mostly impact the normalization of the passbands cancels out. In order to illustrate the impact of the uncertainties in our passband determination in this case, we modeled the spectrum of 6 calibration LEDs as Gaussian shapes centered on the central wavelength of each filter with a full-width half-maximum of 7% in wavelength. To simulate the effect of the passband recalibration on LED observations, we propagate the uncertainties on the *ratios* of broadband fluxes between the LEDs and G191B2B. The results are presented in Table 4. As expected, most broadband error sources cancel out, resulting in an accuracy of the order of 1 permil, matching the requirements for the StarDICE experiment.

In contrast, the sensitivity to wavelength calibration generally increases in a way that depends on the spectra of the LEDs. The flux of LEDs whose spectrum overlaps with the edges of the filters are more strongly affected by wavelength calibration errors than LEDs whose spectrum is largely contained in the filter passband. The design of the StarDICE artificial star includes both cases, with the idea that overlapping LEDs can provide a handle to test (or correct) for filter front errors. Here we report sensitivity for non-overlapping LEDs assuming no specific correction.

6. Conclusion

We determined the response of the 16" StarDICE telescope using a collimated beam projector (CBP) powered by a tunable laser. Our procedure involved three main steps. In the first step, we measured the throughput of the CBP with a wavelength sampling of 1 nm between 350 and 1100 nm by illuminating a calibrated solar cell. We then used the calibrated beam to map the response of the StarDICE telescope at all wavelengths and several positions on its primary mirror. Lastly, we interpolated between the sample points to synthesize the equivalent response of the telescope to the illumination of its full pupil.

A key aspect of calibrating the CBP beam is that the sensitive area of the photodiode is large enough to cover the beam entirely. While the measurement is simple in its principle, special care must be given to several aspects of the setup and analysis to reach the required level of accuracy. Most notably: (1) the laser beam must be filtered to improve the purity of its wavelength

Table 4: Uncertainties in the flux of G191B2B after recalibration by observation of narrow-spectrum LEDs centered on the filter passband.

Source	u	g	r	i	z	y
	[%]	[%]	[%]	[%]	[%]	[%]
StarDICE	0.2	0.3	0.2	0.2	0.5	1.8
ϵ_{SC}	0.4	0.1	0.1	0.1	< 0.1	0.1
CBP	0.5	0.5	1.1	< 0.1	< 0.1	< 0.1
Stat (total)	0.7	0.6	1.1	0.2	0.5	1.8
Scattered light	< 0.1	0.1	< 0.1	< 0.1	< 0.1	< 0.1
Repeatability	< 0.1	< 0.1	0.1	< 0.1	< 0.1	< 0.1
Linearity	< 0.1	< 0.1	< 0.1	< 0.1	< 0.1	< 0.1
Contamination	0.1	0.1	< 0.1	< 0.1	< 0.1	< 0.1
Mirror sampling noise	< 0.1	< 0.1	< 0.1	< 0.1	< 0.1	< 0.1
NIST photodiode	0.1	0.1	< 0.1	< 0.1	< 0.1	0.1
Solar cell temperature	< 0.1	< 0.1	< 0.1	< 0.1	< 0.1	0.6
Wavelength calibration [†]	0.3	0.5	0.6	1.1	0.9	1.4
Syst (total)	0.3	0.5	0.6	1.1	0.9	1.5
Total	0.8	0.8	1.3	1.1	1.1	2.4

Notes. [†]The impact of wavelength calibration on led-calibrated fluxes depend significantly on the exact spectrum of the LEDs. The numbers presented come from a simulation of a realistic case, but the numbers for actual LEDs may differ.

composition, even with the mitigation measures we adopted, unavoidable contamination had to be subtracted in the analysis; (2) the setup must minimize scattered light which affects differently the calibration solar cell and the calibrated telescope; (3) achieving sufficient signal to noise ratio in the solar cell implies to fight with a high level of $1/f$ noise (pink noise).

To deal with this issue, we selected a solar cell with high impedance, and grouped the light deposit in short bursts to reduce the pink noise effects while illuminating the solar cell. These bursts were separated by dark periods. Using good synchronization in time between the bursts and the photocurrent measurements, we could estimate the dark current contribution and correct it. Additionally, we increased the collected flux in the solar cell by selecting a larger pinhole, inducing a small but measurable change in the chromatic throughput of the CBP, which must be accounted for. We did not find significant non-linearities in our measurement chain. Repeating the measurements allowed us to identify a slight evolution in the throughput, which was easily corrected.

Most of the measurement time is spent in mapping the telescope response which scales linearly with the number of filters, resolution in wavelength, and number of mirror samples taken. Our main 4-positions analysis, which yields subpercent precision on the synthesized passbands involved about 30 000 images. The complete dataset, including runs for the characterization of systematics, pinhole inter-calibration, and focal plane measurements, close 200 000 images. With our fully automated setup, collecting this dataset required 7 days of uninterrupted operation.

Our analysis allowed us to determine filter fronts with a precision of about 0.2 nm, to accurately measure out-of-band leaks at a relative level of 10^{-3} and revealed an unexpected and strong dependency of the mirror reflectivity with the incidence angle in the UV. As a result, we were able to show through simulations that the uncertainties in our determination of the telescope

passbands will not contribute more than 1% uncertainty in the measurement of broadband flux with StarDICE after calibration by observations of the artificial star.

The results presented in this paper also serve as a proof of concept for the Rubin CBP, specifically designed for measuring the LSST passbands at the Vera C. Rubin Observatory. Although scaling this setup from a 16" to a 8 m telescope will be challenging in many regards (more optical surfaces inducing ghosts, larger filters, more sensors), similar numbers are to be expected for the determination of LSST passbands if the necessary amount of calibration time is provided. This calibration will allow an accurate interpretation of the flux ratios between the established photometric standards and the SNe Ia observed to map the Universe's expansion history. On the other hand, developing a traveling version of the CBP is currently undergoing (Sommer et al. 2024) to calibrate the filter transmissions of ongoing and future SNe Ia surveys.

References

- Betoule, Antier, Sarah, Bertin, Emmanuel, et al. 2023, A&A, 670, A119
- Betoule, M. 2022, betoule/logic_timer: v1.0.1
- Betoule, M., Kessler, R., Guy, J., et al. 2014, Astronomy & Astrophysics, 568, A22
- Bohlin, R. C., Hubeny, I., & Rauch, T. 2020, AJ, 160, 21
- Brout, D., Sako, M., Scolnic, D., et al. 2019, ApJ, 874, 106
- Brout, D., Scolnic, D., Popovic, B., et al. 2022, The Astrophysical Journal, 938, 110
- Brownsberger, S., Zhang, L., Andrade, D., & Stubbs, C. W. 2022, Journal of Astronomical Instrumentation, 11, 2250002
- Coughlin, M., Abbott, T. M. C., Brannon, K., et al. 2016, in Society of Photo-Optical Instrumentation Engineers (SPIE) Conference Series, Vol. 9910, Observatory Operations: Strategies, Processes, and Systems VI, ed. A. B. Peck, R. L. Seaman, & C. R. Benn, 99100V
- Coughlin, M., Deustua, S., Guyonnet, A., et al. 2018, in Observatory Operations: Strategies, Processes, and Systems VII
- Dhawan, S., Goobar, A., Smith, M., et al. 2022, MNRAS, 510, 2228
- Green, M. A. 2008, Solar Energy Materials and Solar Cells, 92, 1305
- Houston, J. M. 2008, NIST Special Publication, 250, 41
- Ingraham, P., Stubbs, C. W., Claver, C., et al. 2016, in Ground-based and Airborne Telescopes VI, ed. H. J. Hall, R. Gilmozzi, & H. K. Marshall, Vol. 9906, International Society for Optics and Photonics (SPIE), 99060O
- Lochner, M., Scolnic, D., Almoubayyed, H., et al. 2022, ApJS, 259, 58
- Lombardo, S., Küsters, D., Kowalski, M., et al. 2017, Astronomy & Astrophysics, 607, A113
- LSST Science Collaboration, Abell, P. A., Allison, J., et al. 2009, arXiv e-prints, arXiv:0912.0201
- Marshall, J. L., Rheault, J.-P., DePoy, D. L., et al. 2013, arXiv e-prints, arXiv:1302.5720
- Moffat, A. F. J. 1969, A&A, 3, 455
- Mondrik, N., Coughlin, M., Betoule, M., et al. 2023, Publications of the Astronomical Society of the Pacific, 135, 035001
- Narayan, G., Matheson, T., Saha, A., et al. 2019, The Astrophysical Journal Supplement Series, 241, 20
- Neveu, J., Brémaud, V., Antilogus, P., et al. 2024, A&A, 684, A21
- Rubin, D., Aldering, G., Betoule, M., et al. 2023, Union Through UNITY: Cosmology with 2,000 SNe Using a Unified Bayesian Framework
- Scolnic, D. M., Jones, D. O., Rest, A., et al. 2018, ApJ, 859, 101
- Shaw, P.-S., Li, Z., Arp, U., & Lykke, K. R. 2007, Applied Optics, 46, 5119
- Sommer, K., Cohen-Tanugi, J., Plez, B., et al. 2024, RAS Techniques and Instruments, 3, 125
- Stubbs, C. W. & Tonry, J. L. 2006, ApJ, 646, 1436
- Woodward, J. T., Shaw, P.-S., Yoon, H. W., et al. 2018, Review of Scientific Instruments, 89, 091301
- Yasuda, N., Tanaka, M., Tominaga, N., et al. 2019, PASJ, 71, 74
- Acknowledgements.* This work received support from the Programme National Cosmology et Galaxies (PNCG) of CNRS/INSU with INP and IN2P3, co-funded by CEA and CNES and from the DIM ACAV program of the Île-de-France region. CWS, EU, and SB are grateful to the US Department of Energy for support under Cosmic Frontier award DE-SC0007881. This paper has undergone internal review in the LSST Dark Energy Science Collaboration. The internal reviewers were Johan Bregeon and Parker Fagrelis. Thierry Souverin is the primary author of the paper, and he contributed to the

hardware assembly, the data taking, the data analysis and the paper edition. Jérémy Neveu is the primary author's advisor and participated to the hardware assembly, the data taking, the data analysis and the paper edition. Marc Betoule is the StarDICE PI and participated to the hardware assembly, data taking, data reduction, lead the pupil stitching analysis and participated to the paper edition. Sébastien Bongard contributed to the logistics, the hardware assembly, the data analysis and the paper edition. Christopher W. Stubbs is the instigator of the CBP concept and he contributed to a large part of the hardware funding, and to the solar cell calibration. Elana Urbach participated to the hardware assembly, the data taking and the solar cell calibration. Sasha Brownsberger participated to the hardware assembly, the data taking, and the solar cell calibration. Pierre Éric Blanc is member of the StarDICE collaboration. Johann Cohen Tanugi is member of the StarDICE collaboration. Sylvie Dagoret-Campagne is member of the StarDICE collaboration. Fabrice Feinstein is member of the StarDICE collaboration. Delphine Hardin is member of the StarDICE collaboration. Claire Juramy is member of the StarDICE collaboration. Laurent Le Guillou is member of the StarDICE collaboration and contributed with software and hardware support. Auguste Le Van Suu is member of the StarDICE collaboration. Marc Moniez is member of the StarDICE collaboration. Éric Nuss (posthumous) is member of the StarDICE collaboration. Bertrand Plez is member of the StarDICE collaboration. Nicolas Regnault is member of the StarDICE collaboration. Eduardo Sepulveda is member of the StarDICE collaboration and contributed with software and hardware support. Kélian Sommer is member of the StarDICE collaboration. All members of the StarDICE collaboration contributed by their general support to the collaboration and to the collaboration review of the paper. The DESC acknowledges ongoing support from the Institut National de Physique Nucléaire et de Physique des Particules in France; the Science & Technology Facilities Council in the United Kingdom; and the Department of Energy, the National Science Foundation, and the LSST Corporation in the United States. DESC uses resources of the IN2P3 Computing Center (CC-IN2P3–Lyon/Villeurbanne - France) funded by the Centre National de la Recherche Scientifique; the National Energy Research Scientific Computing Center, a DOE Office of Science User Facility supported by the Office of Science of the U.S. Department of Energy under Contract No. DE-AC02-05CH11231; STFC DiRAC HPC Facilities, funded by UK BEIS National E-infrastructure capital grants; and the UK particle physics grid, supported by the GridPP Collaboration. This work was performed in part under DOE Contract DE-AC02-76SF00515.

Appendix A: Ghost photometry

Let be $G_0(\lambda)$ the quantity of light collected in the main spot, and $G_n(\lambda)$ the quantity of light collected in the ghost of order n . The ratio of the 1st order ghost $G_1(\lambda)$ over the main spot $G_0(\lambda)$ is:

$$K_{G_1/G_0}(\lambda) = \frac{G_1(\lambda)}{G_0(\lambda)}. \quad (\text{A.1})$$

We measure $G_1(\lambda)$ with the 75 μm pinhole where it is well separated from $G_0(\lambda)$. We build a mask with the expected ghost shape like, shown in Figure 33, and we fit its best position on the image. To estimate the background at this position, we assume that the main spot exhibits vertical spatial symmetry and measure the flux within a symmetric mask at the vertically opposite position relative to the main spot. $G_1(\lambda)$ is the sum of the ADUs in the ghost mask after background subtraction. On the other hand, $G_0(\lambda)$ is measured with the baseline photometry detailed in Section 4.4.

This study is pursued for the 3 runs of dataset No. 4 and 2 runs of dataset No. 2 from Table 2. The results obtained for $K_{G_1/G_0}(\lambda)$ are shown in Figure A.1, for which the mean spline is displayed in the third panel of Figure 35.

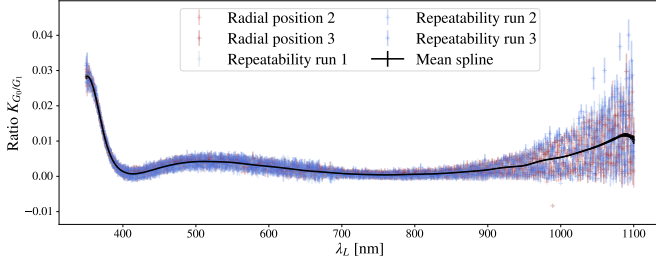


Fig. A.1: Ratio $K_{G_1/G_0}(\lambda)$ with respect to λ_L . The mean spline goes through the five datasets.

This method allows for estimation of $G_1(\lambda)$, but we must investigate the contribution of ghosts of higher order $G_{n>1}$. Because of the faint intensity of these orders, the method described above cannot be performed, so we estimate their contribution from the 1st order ghost analysis. Let be $R_{\text{win}}(\lambda)$ the reflection coefficient at the interface air-window, and $R_{\text{ccd}}(\lambda)$ the reflection coefficient at the interface air-CCD. We know the transmission of the window $T_{\text{window}}(\lambda)$ from manufacturer datasheets, so we can infer $R_{\text{win}}(\lambda)$:

$$R_{\text{win}}(\lambda) = 1 - T_{\text{window}}(\lambda), \quad (\text{A.2})$$

which is represented as the blue curve in Figure A.2. We define $F(\lambda)$ the flux collected in the camera, $G_0(\lambda)$ the quantity of light collected in the main spot, and $G_n(\lambda)$ the quantity of light collected in the ghost of order n . $G_0(\lambda)$ and $G_n(\lambda)$ are a function of $F(\lambda)$:

$$G_0(\lambda) = (1 - R_{\text{win}}(\lambda))^2 \times (1 - R_{\text{ccd}}(\lambda)) \times F(\lambda), \quad (\text{A.3})$$

$$\begin{aligned} G_n(\lambda) &= G_0(\lambda) \times [R_{\text{ccd}}(\lambda)R_{\text{win}}(\lambda) + R_{\text{ccd}}(\lambda)(1 - R_{\text{win}}(\lambda))R_{\text{win}}(\lambda)]^n \\ &= G_0(\lambda) \times [2R_{\text{ccd}}(\lambda)R_{\text{win}}(\lambda) - R_{\text{ccd}}(\lambda)R_{\text{win}}(\lambda)^2]^n. \end{aligned}$$

The sum of all the ghosts $G_{n>0}(\lambda)$ is defined as ⁷:

$$\begin{aligned} G_{n>0}(\lambda) &= \sum_{n=0}^{n \rightarrow \infty} G_n(\lambda) - G_0(\lambda) \\ &= G_0(\lambda) \times \sum_{n=0}^{n \rightarrow \infty} ([2R_{\text{ccd}}(\lambda)R_{\text{win}}(\lambda) - R_{\text{ccd}}(\lambda)R_{\text{win}}(\lambda)^2]^n - G_0(\lambda)) \\ &= G_0(\lambda) \times \left(\frac{1}{1 - [2R_{\text{ccd}}(\lambda)R_{\text{win}}(\lambda) - R_{\text{ccd}}(\lambda)R_{\text{win}}(\lambda)^2]} - 1 \right), \end{aligned} \quad (\text{A.4})$$

and the sum of the ghost of order higher than 1 is defined as:

$$G_{n>1}(\lambda) = G_{n>0}(\lambda) - G_1(\lambda). \quad (\text{A.5})$$

As we measure the photometry of the 1st order ghost $G_1(\lambda)$, we want to verify that the ghosts of higher orders $G_{n>1}(\lambda)$ are negligible. Using the Equations A.1, A.3 and A.4, we can compute $R_{\text{ccd}}(\lambda)$:

$$R_{\text{ccd}}(\lambda) = \frac{K_{G_1/G_0}(\lambda)}{R_{\text{win}}(\lambda)(2 - R_{\text{win}}(\lambda))}, \quad (\text{A.6})$$

reported as the red curve in Figure A.2.

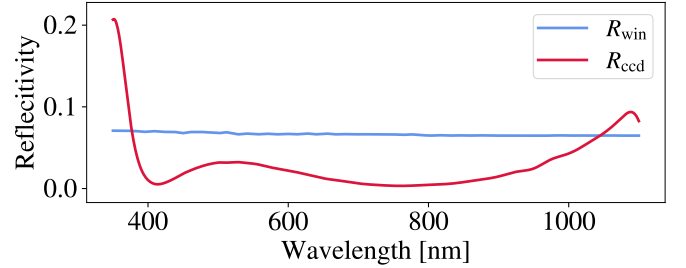


Fig. A.2: Reflectivities of the CCD $R_{\text{ccd}}(\lambda)$ in red, and the camera window $R_{\text{win}}(\lambda)$ in blue, both against the wavelength.

We measured $G_1(\lambda)$ with photometry, and estimate $G_{n>1}$ with the equations above. We show the ratio $K_{G_{n>1}/G_0}$ in Figure A.3, and we see that $K_{G_{n>1}/G_0}$ is always below the per mil level. Since $G_{n>1}$ contribute for less than a per mil of $G_0(\lambda)$, we decide to neglect it.

⁷ If $|q| < 1$, the serie $(\sum_{n=0}^m q^n)_{m \in \mathbb{N}}$ strictly converge and $\sum_{n=0}^{\infty} q^n \equiv \lim_{m \rightarrow \infty} \sum_{n=0}^m q^n = \frac{1}{1-q}$

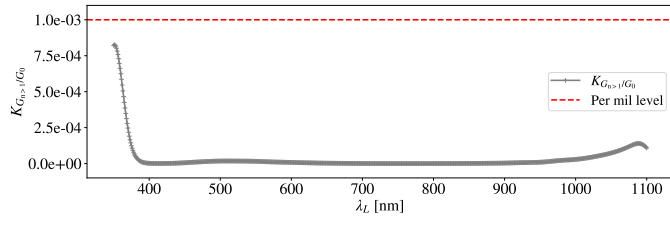


Fig. A.3: Ratio $K_{G_{n>1}/G_0}(\lambda)$ (which corresponds to the sum of the ghosts at order higher than 1 $G_{n>1}(\lambda)$ over $G_0(\lambda)$) with respect to λ_L .